

TAILORING NONLINEAR TEMPERATURE PROFILE IN LASER-MATERIAL PROCESSING

A DISSERTATION SUBMITTED TO
THE GRADUATE SCHOOL OF ENGINEERING AND SCIENCE
OF BILKENT UNIVERSITY
IN PARTIAL FULFILLMENT OF THE REQUIREMENTS FOR
THE DEGREE OF
DOCTOR OF PHILOSOPHY
IN
ELECTRICAL AND ELECTRONICS ENGINEERING

By
Denizhan Koray Kesim
March 2019

Tailoring nonlinear temperature profile in laser-material processing

By Denizhan Koray Kesim

March 2019

We certify that we have read this dissertation and that in our opinion it is fully adequate, in scope and in quality, as a dissertation for the degree of Doctor of Philosophy.

Fatih Ömer İlday(Advisor)

Oğuz Gülseren

Ömer Morgül

Clara Saraceno

Ali Bozbey

Approved for the Graduate School of Engineering and Science:

Ezhan Karaşan
Director of the Graduate School

ABSTRACT

TAILORING NONLINEAR TEMPERATURE PROFILE IN LASER-MATERIAL PROCESSING

Denizhan Koray Kesim

Ph.D. in Electrical and Electronics Engineering

Advisor: Fatih Ömer İlday

March 2019

Ablation cooled material removal opened up great opportunities for understanding nonlinear processes. Especially using lasers as a tool to tailor nonlinear temperature gradient of material and engineering them to achieve effects such as high ablation efficiency, speed, and low collateral damage.

Numerical simulations showed such engineering of the temperature gradient of material is possible for any repetition rate falling inside the ablation cooling regime. Two temperature model is used to investigate the effects of repetition rate, pulse energy, and burst duration. Simulations suggest ablation can continue indefinitely as burst duration increases. They also suggest there is an optimum pulse energy for any repetition rate in terms of efficiency of ablation regarding the material.

The results of the simulations are confirmed by experiments using lasers with 1.6 GHz, 1.46 GHz, and 13 GHz repetition rate on biological and technical materials. The ablation threshold for a single pulse is lowered 100 times compared to our previous publication.

Finally, related studies that can build upon the shown results are presented. A new thin-disk laser oscillator scheme is proposed that implements mode-locking regimes already established in fiber lasers. Dissipative soliton and similariton simulation results are promising for further studies. They can achieve high energy pulses with the help of nonlinear effects instead of limited by it. Then, a new computer generated hologram algorithm is explained where hundreds of layers can be generated from a single hologram. The algorithm utilizes diffusion as a tool to increase the degree of freedom which in turn decreases the cross-talk between layers.

Keywords: burst mode, laser material processing, ablation cooling, ultrashort pulses, nonlinear system, thermal profile.

ÖZET

DOĞRUSAL OLMAYAN SICAKLIK PROFİLİNİN LAZER MATERYAL İŞLEME İÇİN DÜZENLENMESİ

Denizhan Koray Kesim

Elektrik Elektronik Mühendisliği, Doktora

Tez Danışmanı: Fatih Ömer İlday

Mart 2019

Ablasyon soğutmalı materyal kaldırma yeni araştırmalar için önemli fırsatları öne çıkardı. Örneğin, doğrusal olmayan işlemleri anlamak ve materyalin sıcaklık profillerini isteğe göre düzenleyebilmek için ultrahızlı lazerler kullanılabilir ve yüksek ablasyon verimi, hız ve düşük istenmeyen hasarlar gibi iyileştirmelere ulaşılabilir.

Sayısal simülasyonlar ise ablasyonla soğutma rejimi içerisindeki tekrar frekanslarında sıcaklık profilini düzenlemenin mümkün olduğunu gösterdi. Tekrar frekansı, atım enerjisi ve küme uzunluğunu araştırmak için çift sıcaklık modeli kullanıldı. Simülasyonlar, ablasyonun küme içerisindeki atım sayısı artıkça süresiz olarak artabileceğini belirlemektedir. Ayrıca, materyaller için her tekrar frekansında en yüksek verimi elde edebileceğimiz bir atım enerjisi olduğunu göstermektedir.

Bu simülasyonların sonuçları yapılan deneyler ile doğrulandı. 1.5 GHz, 1.46 GHz ve 13 GHz tekrar frekanslarına sahip üç farklı lazer sistemiyle organik olan ve olmayan materyaller üzerinde denemeler yapıldı. Önceki çalışmalarımıza göre ablasyon için gerekli olan atım enerjisi 100 kat daha düşürüldü.

Son olarak, sunulan sonuçlarla alakalı olarak araştırılan çalışmalar gösterildi. Bunlardan biri fiber lazerlerde yaygın olarak kullanılan kip kilit durumlarının ince disk lazer salıngaçlarına uyarlanmasıdır. Dissipative soliton ve similariton durumlarının simülasyon sonuçları ileriki çalışmaların önünü açmıştır. Böylece yalnızca salıngaç kullanarak yüksek atım enerjilerine ulaşılabilir. Diğer bir çalışma da bilgisayarda üretilen hologramlar için geliştirilmiş yeni bir algoritma sayesinde yüzlerce katmanlı üç boyutlu görüntüler tek katmanlı hologram içerisine yazılabilmektedir. Bunun için de her katman hesaplanırken yayınma eklenmiş, böylece serbestlik derecesi artırılmıştır. Sonuç olarak da aşılması zor olan katmanlar arası çapraz konuşma azaltılmıştır.

Anahtar sözcükler: küme modu, lazer materyal işleme, ablasyon soğutma, ultra hızlı atımlar, doğrusal olmayan sistem, sıcaklık profili.

Acknowledgement

I would like to thank Fatih Ömer İlday for being my advisor and leading me in my research. Thanks to him, I can truly appreciate scientific work.

I specially want to express my gratitude to Parviz Elahi and Hamit Kalaycıođlu for their endless patience with me. Thanks to their knowledge and discussions. This thesis wouldn't be possible without their assistance and hard work.

I would like to thank my parents, Servet Kesim and Bülent Kesim, and my sister, Yaprak Öykum Kesim for their endless love and support. Their influence shaped me to be the person I am. Their place in my life is irreplaceable.

Last, but not least, I would like to express my great appreciation to Özgün Yavuz, Ahmet Turnalı, Ghaith Makey, Tasnim Arony, Gizem Gençođlu, Onur Tokel, and Murat Sözen for many enjoyable conversations. My special thanks are extended to Ozan Yasar, Kerem Ali Dođan and Çađatay Altınok for their most valuable friendship and helping me to endure challenges of life.

I would like to acknowledge TÜBİTAK grant 117F149 for funding me through this thesis.

Contents

1	Introduction	1
1.1	Laser Material Processing	3
1.2	Ultrafast Laser Material Ablation As A Nonlinear Process	5
1.3	Ablation Cooled Material Processing	6
1.4	Engineering Heat Distribution Inside Material	8
2	Simulations	9
2.1	Toy Model	9
2.2	Two Temperature Model	11
2.3	Scaling of Ablation Cooled Material Processing	13
2.3.1	Scaling of Ablation with Number of Pulses	13
2.3.2	Scaling of Pulse Energy with Repetition Rate	15
2.4	Efficiency of Ablation	16
2.4.1	Tailoring Heat Distribution Inside the Material	18
3	Experiments	23
3.1	Materials	24
3.2	Laser Systems	25
3.2.1	1.6 GHz experiments	26
3.2.2	1.46 GHz experiments	27
3.2.3	13 GHz experiments	28
3.3	Analysis	29
4	Results & Discussion	30
4.1	Verification of Simulation Claims on Silicon	30
4.1.1	1.6 GHz Results	30

4.1.2	1.46 GHz results	31
4.1.3	13 GHz results	32
4.2	Ultrafast ablation of Dentin Suitable for Real World Applications	33
4.2.1	1.46 GHz results	34
4.3	Discussion	34
5	Approaching from Broader Perspective	44
5.1	Adapting Mode-locking Regimes to Thin Disk Lasers	45
5.2	3D Projection from Single Hologram Layer	49
6	Conclusion	55
A	Laser Systems	64
A.1	1.6 GHz Non-PM System	64
A.2	1.46 GHz PM System	66
A.3	13 GHz Prechirped System	67
B	Burst Envelope Shaping by Modelled Amplifiers	73
B.1	MATLAB Implementation	74

List of Figures

1.1	Any pulse will penetrate material for some depth and increase its temperature. If the temperature exceeds ablation threshold, material will be ablated for any depth that exceeds.	4
1.2	Ablation with smaller, closely packed pulses. Wasted energy and residual heat are reduced significantly.	7
2.1	40 pulses repeated at 400 MHz is simulated with TTM model. Electrons absorb the energy from pulses (blue) and transfers that energy to the lattice (red). When lattice temperature exceeds ablation threshold, it is removed from the simulation and considered ablated.	14
2.2	The ablated depth increases linearly with number of pulses for both 1.6 GHz and 6.4 GHz. Ablated volume per pulse for 6.4 GHz case is lower but the total efficiency is not. Efficiency of ablation is investigated later.	15
2.3	Calculated and simulated most efficient pulse energy for each pulse repetition rate.	16
2.4	There is a peak of efficiency for each repetition rate. Also, the peak values for each of them increases for higher repetition rates. Efficiency values are normalized for maximum efficiency.	17
2.5	Surface temperature gradient before (blue) and after (red) 20 ps of a burst. Burst has 1.6 GHz pulse repetition rate with 160 pulses. Each pulse has 400 nJ energy.	19

2.6	Temperature of surface (red), 1 μm below surface (green) and electrons at surface (blue). Pulse repetition rate is 1.6 GHz with 982 nJ pulses. Ablation only starts after lattice temperature reaches to 15000 K.	20
2.7	Simulation run for 6.4 GHz repetition rate pulses. Number of pulses is scaled to 640 to keep the burst duration same as other simulations. Subsurface temperatures are reduced significantly compared to 1.6 GHz case.	21
2.8	Contour of temperatures over 0.5 ns. The surface of the material is on the left side. After a pulse arrives, it ablated some of the material which resets the temperature to room temperature (300 K).	22
2.9	Residual heat after a single burst for different pulse energies. Repetition rate is 3.2 GHz.	22
3.1	General setup for experimental laser systems.	23
3.2	One stage of repetition rate multiplier. The length of the fibers are adjusted such that frequency of the pulse train doubles at each stage while the pulse energy is decreased by half.	26
4.1	SEM images of silicon samples. Each was processed with a single burst containing a various number of pulses per burst. Pulse energy is kept constant at 50 nJ	36
4.3	SEM images of silicon experiment. One burst per spot with 25 nJ pulse energy, 730 pulses	37
4.4	LSM image of one burst per spot with 25 nJ pulse energy, 730 pulses. The depth of the holes are measured as 9 μm while the diameter is 5 μm	38
4.5	SEM images for 160 μJ burst energy with 10-80 nJ pulse energies. Number of pulses per burst are adjusted to keep the burst energy constant.	39
4.6	SEM image and LSM measurement of silicon processed with bursts containing 24000 pulses with 5 nJ energy each.	39

4.8	Drilling 200 μm thick silicon with 15 nJ pulses. Each burst consists of 6000 pulses. Scanning speed is constant at 2 m/s. 1, 2, 5 and 10 passes are applied on different samples. SEM images for them are (a), (b), (c) and (d) respectively.	41
4.9	Ablation of dentin with 25 nJ pulses, 730 pulse per burst. Helix pattern is applied with 4 mm diameter shown in (a). Only the center of the pattern achieved ablation. Rest of the tissue remained untouched. The depth of the hole is measured to be 20 μm from LSM measurement in (b).	42
4.10	Another dentin sample 25 nJ pulses, 730 pulse per burst. Same helix pattern is applied with 4 mm diameter. Center of the pattern as well as a line were ablated without any thermal damage. Bottom surface of the sample stays flat, supporting our deduction of ablation without heating.	43
5.1	Passive Multipass cavity for discrete dissipative soliton adapted for TDL	46
5.2	Phase space of a single roundtrip around passive multipass cavity after the pulse stabilizes.	47
5.3	Dissipative soliton TDL: temporal (left) and spectral (right) shape of pulses extracted at the position in the resonator where the spectrum is broadest. The numerically dechirped and nearly transform-limited pulse is indicated in orange color. The chirp of the spectrum is indicated in green. The spectral shape obtained is characteristic for the all-normal dispersion regime. Figure taken from [50]	48
5.4	Active multipass cavity for discrete similariton laser adapted to TDL.	49
5.5	Phase space plot of discrete similariton after the pulse stabilizes.	50
5.6	Similariton TDL: Temporal (left) and spectral (right) shape of pulses extracted after the spectrally shaped output coupler. The numerically dechirped and nearly transform-limited pulse is indicated in orange color. The chirp of the spectrum is indicated in green. Figure taken from [50]	51

5.7	Flowchart of the proposed CGH algorithm. Fourier holograms of source images are calculated independently after preprocessing. Then, phases of each image are superimposed with phases of any desired FZPs. Finally, superimposing in complex form and taking the kinoform of the result gives us a single Fresnel hologram capable of projecting multiple planes.	52
5.8	Optical Reconstruction of “BILKENT UNIV” with SLM. Letters are ordered from last to first with respect to SLM. The scale at the corner of each image is 5 mm distances from SLM can be seen below each image.	53
5.9	Computational reconstruction of 100 layers of a space ship by simulating a 4K SLM. Each layer is simulated at their focal point and then combined in 3D computationally.	54
A.1	Schematic of DM oscillator.	64
A.2	Spectrum of the output of 100 MHz DM oscillator.	65
A.3	The general schematic of the 1.6 GHz laser. Amplifiers are seeded by 100 MHz DM oscillator. After stretching the pulses, rep-rate multiplier is used to increase the pulse repetition rate to 1.6 GHz. AOM is modulated with an arbitrary waveform generator to compensate for gain depletion.	68
A.4	In the final stage, two double clad amplifiers are cascaded. The first one amplifies up to 5 W average power with a wavelength stabilized 18 W diode. Second one is coupled with two 55 W 976 nm diodes to achieve 52 W average power.	69
A.5	The burst envelope for 1000 pulses per burst with 100 nJ pulses.	69
A.7	1.46 GHz laser schematic. Amplifier stages are seeded with 89 MHz ANDi oscillator. Power at each stage can be seen above.	70
A.9	13 GHz laser schematic. Amplifier stages are seeded with 100 MHz ANDi oscillator. Power at each stage can be seen above.	71
A.10	The burst envelopes for 2000 pulses per burst for 50, 90 and 120 nJ pulse energies after modulating the AOM for modeled amplifier stages.	71
A.11	Autocorrelation of the output pulses at 50 nJ.	72

List of Tables

3.1	The common parameters between laser systems is their central wavelegth at 1035 nm. Also, they are all fiber based master oscillator power amplifier systems.	25
-----	--	----

Chapter 1

Introduction

The invention of the laser is one of the most consequential technological outcomes of the development of quantum theory. Following their invention in 1960 [1], today, lasers are ubiquitously applied, from diverse scientific applications [2-8], to industry [9], defense [10-12] and medical fields [13-16]. Given that the coherent light output of a laser can be focussed tightly, it can be used to create extremely high energy densities. This property has led to a broad class of laser-material interactions that constitute one of the major application areas for lasers, ranging from cutting, drilling, micro-structuring, surface texturing and functionalization of all sorts of materials, including, particularly in the last decade, various forms of additive manufacturing. A large variety of lasers are being used in such applications, but in terms of the physical processes involved in their interactions with materials, probably the most important property is the temporal profile of the laser's emission. In this sense, lasers can be broadly categorized into those producing a continuous or quasi-continuous (with variations in the microsecond scale or slower) regime (in short, CW), production of pulses that have durations in the nanosecond range and the so-called ultrafast lasers producing ultrashort pulses, which typically refers to few picoseconds and femtosecond pulse durations. The last of these has been drawing the greatest attention in recent decades because it offers processing of materials with a precision that far exceeds those of nanosecond and CW lasers. The removal of material by ultrashort pulses is a

highly nonlinear, explosive process that takes place far from thermal equilibrium and it is generally referred to as ultrafast ablation.

Ultrafast ablation allows processing of virtually any type of material, from strongly reflecting ultra-hard, from brittle to heat sensitive, from metals to semiconductors to living tissue, with unparalleled excellent precision. However, it remains a relatively niche method of laser-material processing due to that the fact ultrafast ablation is energy inefficient and prolonged process. After discussing the physical reasons behind these difficulties, this thesis builds upon a novel technique that has been introduced recently, namely that of ablation-cooled laser-material removal [17]. In simple terms, this approach can be regarded as engineering the temperature gradient created on the material towards achieving high ablation rates and efficiencies at high average powers and pulse repetition rates without inadvertently causing heat accumulation at the target material. One of the critical consequences of this approach turns to be that ablation can occur with pulses that have energies far below the threshold energy that is nominally required. This, in turn, makes entirely new, more practical and lower cost laser designs possible, in addition to negating the weaknesses of femtosecond ablation such as slow processing speeds and low energy efficiencies. The rest of this thesis discusses several concepts that may be key to developing such a new generation of ultrafast lasers that, in turn, could be utilized in ablation-cooled laser-material processing.

In Section 5.1, the viability of different mode-locking regimes in thin-disk lasers is investigated. The longer-term perspective is that thin disk lasers are capable of supporting average powers in the kW range, which could represent oscillator-only solutions that bypass the need for additional amplifiers for ultrafast laser processing. Dissipative soliton and similariton schemes are investigated through simulations.

One of the long-term applications of ablation-cooled laser-material processing is its potential application to 3D printing using the method of two-photon polymerization. Currently, this method is the most precise approach with the

highest resolution (close to 100 nm). However, it requires point-by-point processing, which is extremely slow. In Section 5.2, we discuss a new method that allows construction of large-volume, high-density 3D projections with a single layer hologram. We demonstrate a record number of layers with good quality and minimal crosstalk. It is conceivable that such a technique would allow 3D printing of the whole object at once with all points being processed at once. However, the pulse energies of the ultrafast lasers typically used for this application would not be sufficient for such parallel processing. The exciting distant possibility is whether the core concept of ablation-cooling can be a generalization to reduce the threshold for a two-photon polymerization process. If so, a future study might combine ablation-cooled laser processing with the 3D hologram generation technique discussed in this chapter to create 3D printed structures all at once. Such an approach would not require beam scanning which limits the speeds, instead of using volumetric laser processing based on currently reachable average powers and pulse energies.

1.1 Laser Material Processing

Lasers have been idealized as perfect cutting tools with surgical precision since their invention [16]. The physics in effect vary with duration of pulses in use. High power continuous wave (CW) lasers are used for cutting through steel by heating and melting the material [18, 19]. Nanosecond lasers differ in that they also lead to ablation, assisted by plasma creation [20]. Trade off here is to sacrifice speed but gain precision and reduce damage induced on the material. Nevertheless, they fall far short of ultrafast lasers in terms of localization of heat and therefore avoidance of collateral heat damage. Both CW and nanosecond lasers have become the industry standard due to their practicality and low costs, despite the damage they induce and much lower precisions compared to ultrafast lasers. Only in the ultrafast regime, surgical precision can be achieved with minimal heating [21]. However, as mentioned above, the ultrafast ablation process is not efficient and requires complex laser systems, not to mention that removal of material is generally much slower than CW or nanosecond lasers.

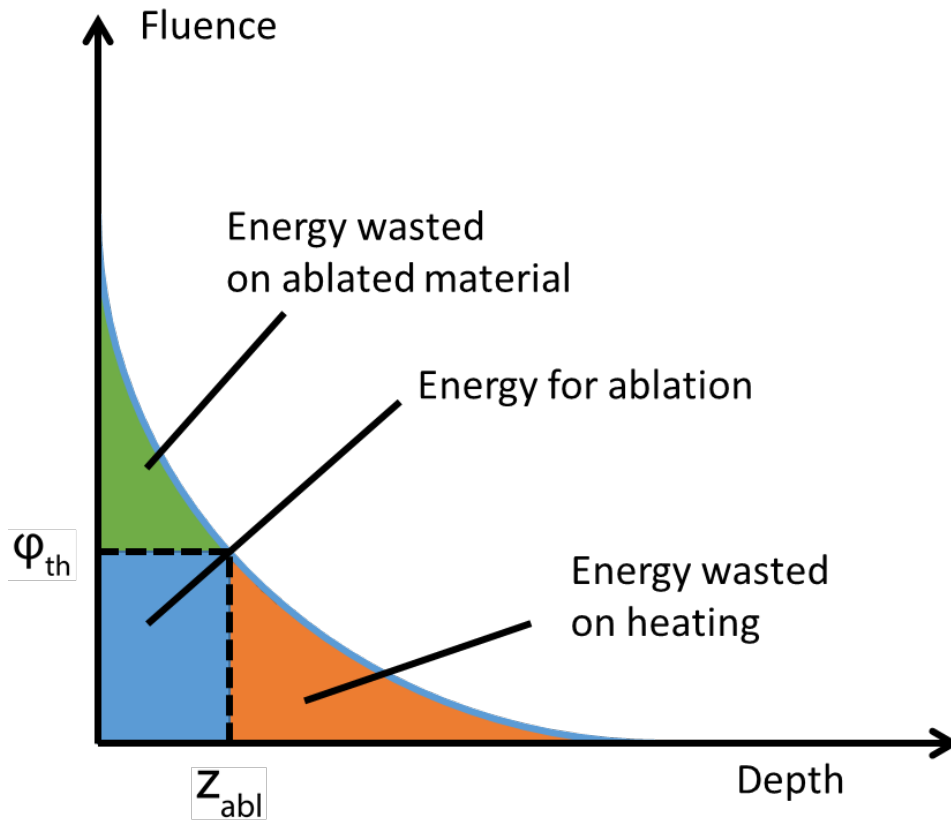


Figure 1.1: Any pulse will penetrate material for some depth and increase its temperature. If the temperature exceeds ablation threshold, material will be ablated for any depth that exceeds.

It is tempting to think that if merely the repetition rate and average power of femtosecond lasers are increased, they lead to high-speed ablation while preserving their excellently precise effects on a material. However, this optimistic thinking turns out to be simplistic. One is confronted with either low speeds for excellent precision, or higher speeds and higher efficiency, that, unfortunately, leads to some heat accumulation. These problems can be traced back to the Beer-Lambert law [22] that governs the absorption of laser light in the target material. In Figure 1.1, energy delivery for a single pulse according to Beer-Lambert law is shown. The material will absorb incoming pulse according to its absorption coefficient and penetration depth. The green area of Figure 1 corresponds to the energy wasted on the ablated material while the orange is corresponding to energy wasted on heating the material after ablation. That leaves us the blue

area which contributes to the ablation itself. To increase ablation depth, we must increase pulse energy exponentially which is not feasible. On top of that, since the accumulated heat on material is often has destructive consequences.

1.2 Ultrafast Laser Material Ablation As A Nonlinear Process

One of the advantages of ultrafast pulses is increased absorption of the material due to nonlinear absorption. When the band gap of the material is larger than the energy of photons of the laser, multiple photons are required to be present at the same point at the same time to ablate [23]. As a result, the fluence on sample needs to be extremely high which necessitate tight focusing and short pulse durations, typically in femtosecond to picosecond range. Only then, those low energy photons can behave like a single higher energy photon which can excite electrons. The primary mechanism for material removal becomes the plasma induced ejection of material instead of melting or vaporization which reduces the heating of the bulk of the target significantly. However, thermal damage continues to be an issue in precision applications.

One major set back was to reaching the peak powers required for nonlinear absorption. Chirped pulse amplification [24], which was awarded Nobel prize in physics in 2018, allowed to reach very high energy pulses while achieving femtosecond duration. By stretching the pulses before amplification and compressing afterward [25], destructive nonlinear effects are significantly reduced. Hence, ultrafast laser material ablation is made possible.

Ultrafast lasers can overcome the heating problem while being quite inefficient [26] and slow [27]. They are preferred in biological application [28] since heating is a bigger issue in tissue. However, speed remains to be a challenge to overcome. So much so that most medical doctors still prefer mechanical tools over lasers. Besides the obvious advantage of tangible feedback they get, mechanical tools

are still faster than lasers in many applications. Unfortunately, lasers are seen as novelty tools that fail to present meaningful superiority. So far, There are a few exceptions to that, mainly ophthalmological applications [29], such as cataract surgery and LASIK.

1.3 Ablation Cooled Material Processing

A significant drawback of femtosecond lasers has always been its low processing speeds. One of the reasons for using nanosecond lasers for most industrial and biomedical applications is its superior processing speeds. However, the quality of ablation of femtosecond laser processing in terms of thermal effects is unprecedented. One way to increase the speed of ablation is to send more pulses per second [30, 31]. Repetition rate can be increased until other unwanted effects such as plasma shielding [32] become prominent.

Recently, we developed ablation cooled material processing [17, 33, 34] to break the ablation speed barrier by structuring the temperature profile of the material with closely packed, weak pulses. Contrary to existing studies at high repetition rates [35, 36] this technique works by lowering the pulse energies proportionally with increased repetition rate. Repetition rates are typically hundreds of MHz to tens of GHz range. Inside the ablation cooled regime, the temperature profile of the material becomes a nonlinear and iterative function of the entire pulse train. If the repetition rate is comparable to the heat diffusion of the material, accumulated heat on the surface reduces the ablation threshold for incoming pulses. When the ablation threshold is reached, each pulse starts to ablate and remove the excess heat from material (Figure 1.2). As a result, total residual heat is not affected by how many pulses we use and efficiency of ablation for each pulse increases. The next pulse now exploits the energy that normally would be wasted on heating since the ablation threshold of heated material drops.

Another advantage of ablation cooled material processing is reducing the collateral damage around the ablated area. Since we are not letting heat diffuse and

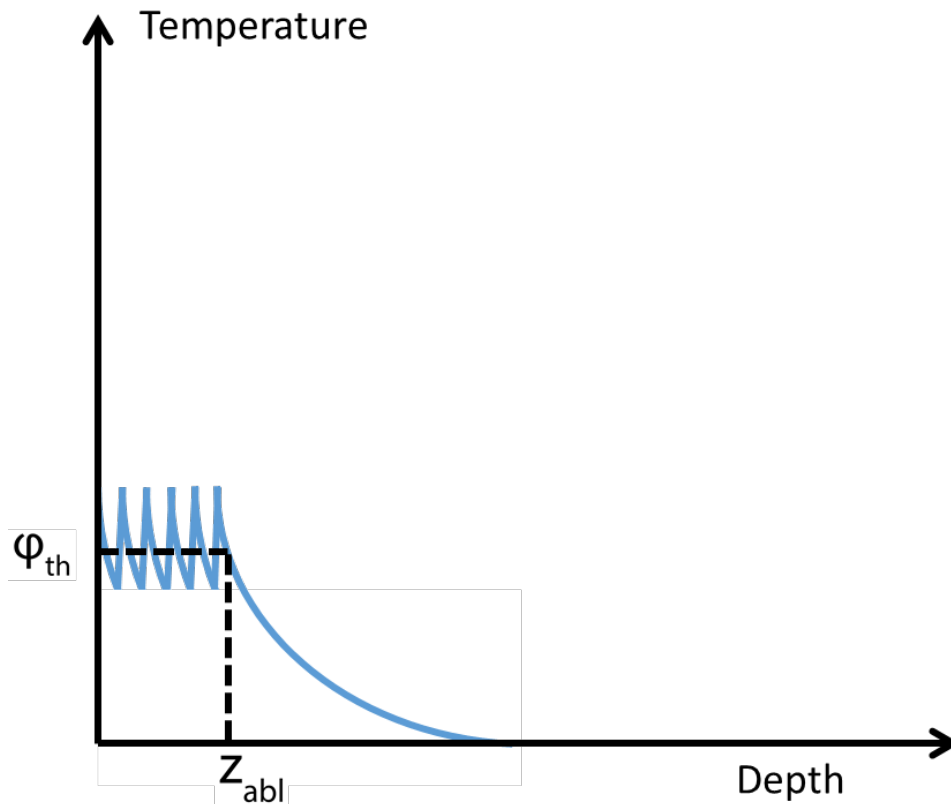


Figure 1.2: Ablation with smaller, closely packed pulses. Wasted energy and residual heat are reduced significantly.

removing excess heat by ablation, the residual heat after the processing ends is drastically reduced. This necessitates very high repetition rates which in turn brings up a new challenge. Even though the pulse energies needed for ablation is reduced significantly, building a high repetition rate laser still requires very high average powers.

Lasers with burst mode operation enable to achieve pulse energies with such high repetition rates by reducing the average power. The burst duration and burst repetition rate offer another degree of freedom for engineering the process. For example, when some parts of the beam fail to ablate even in ablation cooled regime, the low duty cycle of bursts can help to cool the material before the next burst arrives while sacrificing speed.

1.4 Engineering Heat Distribution Inside Material

The idea of reducing the ablation threshold via femtosecond laser-induced heat presents an engineering challenge. Increasing the fluence would remove more volume but also increase the heating. On the other hand, if the fluence is not able to achieve ablation with a given repetition rate, all of the deposited energy will contribute only to heating. The balance between the repetition rate of pulses and the fluence of each pulse within a burst is essential for maximum ablation with minimum heating.

This thesis proposes to engineer the heat distribution inside the material to achieve this. First, the effect of repetition rate and fluence are simulated in Chapter 2. Then, the results of the simulations are tested on silicon and dentin using three custom built lasers with different repetition rate and optics in Chapter 3. In Chapter 4, the results of the experiments are analyzed using a scanning electron microscope and a laser scanning microscope.

Chapter 2

Simulations

Ultrafast laser material processing can be modeled and simulated to confirm interpretations and make further predictions. A toy model was constructed to explore the implications of ablation cooled regime. Three claims are made Two temperature model (TTM) is used for most of the simulations for investigating the efficiency and scaling of ablation cooled material processing. The effects of the number of pulses per burst, repetition rate, and pulse energy are investigated for better efficiency and lower residual heat on the material. Finally, the heat distribution profile is examined during and after ablation.

2.1 Toy Model

A toy model is used to demonstrate the ablation cooled regime. Claim 1 was also explained in [33] while the claim 2 and 3 are modified as extensions of this work. Each pulse is assumed to increase the temperature by a fixed ΔT instantaneously. After that, material cools with $1/\sqrt{\tau_0 + t}$ where τ_0 is the characteristic thermal relaxation time. Then, cooling of the surface after pulse can be written as,

$$T(t) = T_0 + \Delta T \sqrt{\tau_0/(\tau_0 + t)} \quad (2.1)$$

This can be extended for n^{th} pulse as,

$$T_n = T_{n-1} + \Delta T \sqrt{\tau_0/(\tau_0 + \tau_R)} = T_{n-1} + \delta T \quad (2.2)$$

where τ_0 is a pulse to pulse separation. Here, δT is defined to simplify the notation.

The first and main claim of ablation cooled material processing is removing the excess heat deposited on material via ablation induced by incoming pulse. It is made possible by increasing the repetition rate of the laser higher than the characteristic thermal relaxation time of the material. The heat deposited on the material can be expressed as,

$$E_{heat} = \alpha(T_c - T_0) \left(1 - \frac{1}{\sqrt{1 + \tau_R/\tau_0}} \right) (N - m) E_p + \alpha(\Delta T - \delta T) m E_p \quad (2.3)$$

where T_0 is the room temperature, T_c is the lattice on surface immediately after ablation, α is the related heat capacity of the material, E_p is the pulse energy and m is the number of pulses required to start ablation which is denoted as,

$$m = (T_c - T_0 - \Delta T + \delta T) / \delta T \quad (2.4)$$

As the repetition rate of the laser increased, limit of the deposited heat, $\lim_{\tau_R/\tau_0 \rightarrow 0} E_{heat}$ goes to 0.

The second claim is linear increase of ablation depth with burst energy. After the first few pulses prepare the material and reduce the threshold for ablation,

each pulse will ablate a fixed amount. So, as more pulses are added to the burst, the ablation process can be extended. The ablation depth can be written as,

$$d_{ablation} = \eta(N - m)E_{pulse} = \eta(1 - m/N)E_{burst} \quad (2.5)$$

where η is the relation between ablation of a single pulse with pulse energy, N is the number of pulses, E_{pulse} is the pulse energy and E_{burst} is the burst energy. Thus, the linear scaling of ablation with the number of pulses is predicted.

Finally, the third claim is to be able to reduce the ablation threshold indefinitely by increasing the number of pulses while in the ablation cooled regime. The temperature of the surface will be increased with each pulse failing to achieve ablation since the thermal relaxation of material is slower than pulse separation within ablation cooled regime. The relation between number of pulses required to start ablation with pulse energy can be rearranged as,

$$\frac{E_{thres}}{E_{pulse}} = 1 + \frac{m - 1}{\sqrt{1 + \tau_R/\tau_0}} \approx m(1 - \tau_R/\tau_0) \quad (2.6)$$

As long as the right hand side is positive, hence falls inside the ablation cooled regime, the pulse energy required for ablation can be lowered which only increases the number of pulses necessary. This is especially important as it eliminates the need for high pulse energy in ultrafast material processing. However, high peak powers are still needed for nonlinear absorption, if the band gap of the material is higher than the energy of photons of processing laser.

2.2 Two Temperature Model

In this model, the energy of photons is absorbed by the lattice of the material. Then, after some time (typically few picoseconds) absorbed energy is coupled to

the electrons. It is a common way to model ultrafast pulse-material interactions. When the energy of electrons, characterized by electron temperature, exceeds the ablation threshold, that part of the material is considered to be ablated and removed from bulk as explained in the toy model. The implementation is based on simulations explained in [17] where an extensive explanation can be found in the supplementary section.

The spot size is assumed to be 100 times the optical penetration depth to satisfy 1D approximation of heat propagation. So, the equation governing TTM [37] can be written as

$$\begin{aligned} C_e \frac{\partial T_e}{\partial t} &= \frac{\partial}{\partial z} \left(k_e \frac{\partial T_e}{\partial z} \right) - G(T_e - T_L) + S, \\ C_L \frac{\partial T_L}{\partial t} &= G(T_e - T_L), \end{aligned} \quad (2.7)$$

where T_e is the electron temperature, T_L is the lattice temperature, C_e is the specific heat capacity of the electrons, C_L is the specific heat capacity of the lattice, k_e is the thermal conductivity of the electrons, ρ is the material density, z is the direction perpendicular to material, G is the electron-phonon coupling parameter and S is the laser heating term:

$$S = (1 - R)\alpha I_o e^{-\alpha z}, \quad (2.8)$$

where R is the surface reflectivity, α is the absorption coefficient and I_o is the laser intensity.

Nickel is chosen to be modeled for TTM in MATLAB which we used for the rest of the simulations. The ablation occurs when any part of the material exceeds 15000 Kelvin. The absorption coefficient for 1 μm wavelength is 6.27×10^7 1/m. Parts of the material that exceeds the ablation threshold is considered to be ablated and removed from the simulation. This is called the critical point phase separation model [38]. We assumed spot sizes much smaller than optical penetration depth which approximates a 1D material model for simulations. Spot

size is assumed to be μm in diameter for all simulations.

100 MHz, 400 MHz, 800 MHz, 1600 MHz, 3200 MHz, and 6400 MHz repetition rates are simulated independently. After plotting and fitting a curve to the results, 4800 MHz repetition rate is simulated to see if the predictions agree with simulations. All simulations are for a single burst with 100 ns duration unless stated otherwise. The number of pulses changes with each simulated repetition rates.

2.3 Scaling of Ablation Cooled Material Processing

In femtosecond laser material processing, pulses are generally considered to be identical from pulse to pulse. However, in ablation cooled regime, each pulse directly effects the next one. As a result, solving the ablated material as a function of the number of pulses is not trivial.

The most intriguing result is the scaling of ablation with a number of pulses without any additional heating effect. The ablated volume can be increased linearly as the number of pulses in each burst increases, as explained in the next section.

Another outcome of the simulations is the need to scale the pulse energy as pulse-to-pulse repetition rate increases which are explained later in this chapter.

2.3.1 Scaling of Ablation with Number of Pulses

The first set of simulations run for 400 MHz repetition rate which should be safely inside the ablation cooled regime. Each pulse by itself will be able to ablate at any material. However, since the repetition rate is high, heat does not have any time to diffuse, which also reduces the ablation threshold for the next pulse.

The temperature under $1 \mu\text{m}$ of the surface stays low for the duration of the burst. Only after the burst ended, it started to rise again. This suggests the ablation itself is keeping the material cool. When there is no more ablation to remove the excess energy from the material, heat diffuses deep inside. It also suggests that burst duration doesn't affect the residual heat deposited into the material which is what is tested next. In Figure 2.1, an example of the simulation can be seen.

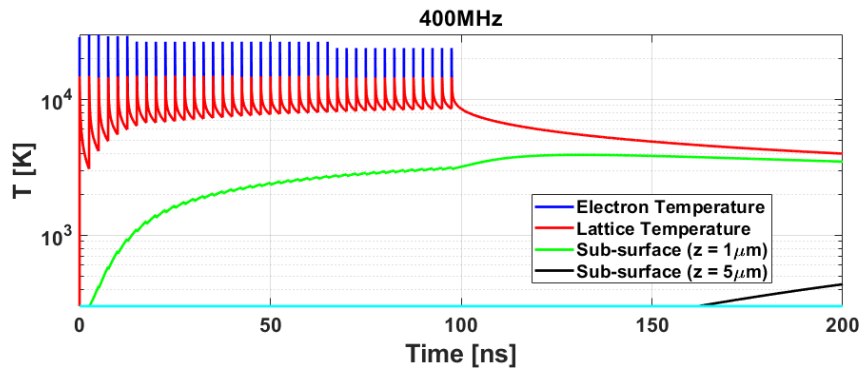


Figure 2.1: 40 pulses repeated at 400 MHz is simulated with TTM model. Electrons absorb the energy from pulses (blue) and transfers that energy to the lattice (red). When lattice temperature exceeds ablation threshold, it is removed from the simulation and considered ablated.

The simulation is repeated for an increasing number of pulses as well as 6.4 GHz repetition rate. The ablated depth is shown in Figure 2.2. The simulations show that ablation can be scaled by simply adding more pulses to the burst. Since the heat distribution reaches a steady state after a number of pulses, each pulse coming after ablates a constant amount of material and pushes the distribution into the material by that amount. Hence, we can continue ablating indefinitely. In practice, there are a few key issues. The most prominent of them is maintaining the focus as we ablate.

On the other hand, the limitations of the TTM model should be addressed. The greatest weakness of the simulation is arguably 1D nature of it. Focused beams are usually Gaussian which has more complex diffusion mechanics. In practice, this translates to failing to ablate at the edges of the focused beam. Thankfully this can be solved by using a top-hat beam at focal point and scanning. For

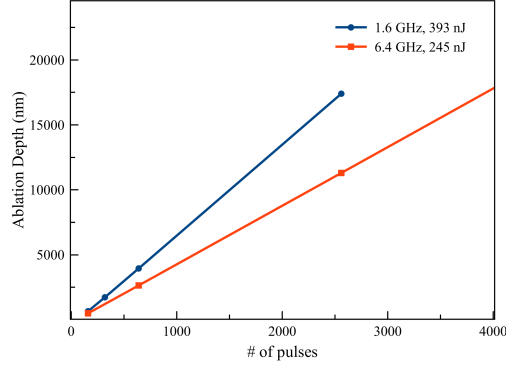


Figure 2.2: The ablated depth increases linearly with number of pulses for both 1.6 GHz and 6.4 GHz. Ablated volume per pulse for 6.4 GHz case is lower but the total efficiency is not. Efficiency of ablation is investigated later.

spot sizes much larger than the penetration depth of the material, heat diffusion can be approximated in 1D. Still, drilling too deep will be an issue. As drilling continues for to deeper depths, the beam will fail to focus due to the edges of the hole. Finally, it is not clear how the heat distribution will be affected by scanning the beam itself. It should be investigated, but it is out of the scope of this thesis.

2.3.2 Scaling of Pulse Energy with Repetition Rate

Since ablation cooled regime requires lower pulse energies, the pulse energy that produces the best efficiency should be predictable. Each pulse is assumed to increase the surface temperature a fixed amount of ΔT . Then, the surface cools with

$$T(t) = \Delta T \sqrt{\frac{1}{1 + t/\tau_0}} + T_0 \quad (2.9)$$

where T_0 is the initial surface temperature, and τ_0 is the characteristic thermal relaxation time. It is assumed the heat diffuses linearly into the material. So we can expect the same kind of behavior to find the most efficient pulse energy for any repetition rate inside the ablation cooled regime since each pulse will see the

same temperature gradient. Although the connection between the two equations is not clear, they can predict the general trend accurately. TTM simulation results are used to fit the equation which will predict the most efficient pulse energies for each repetition rate as seen in Figure 2.3.

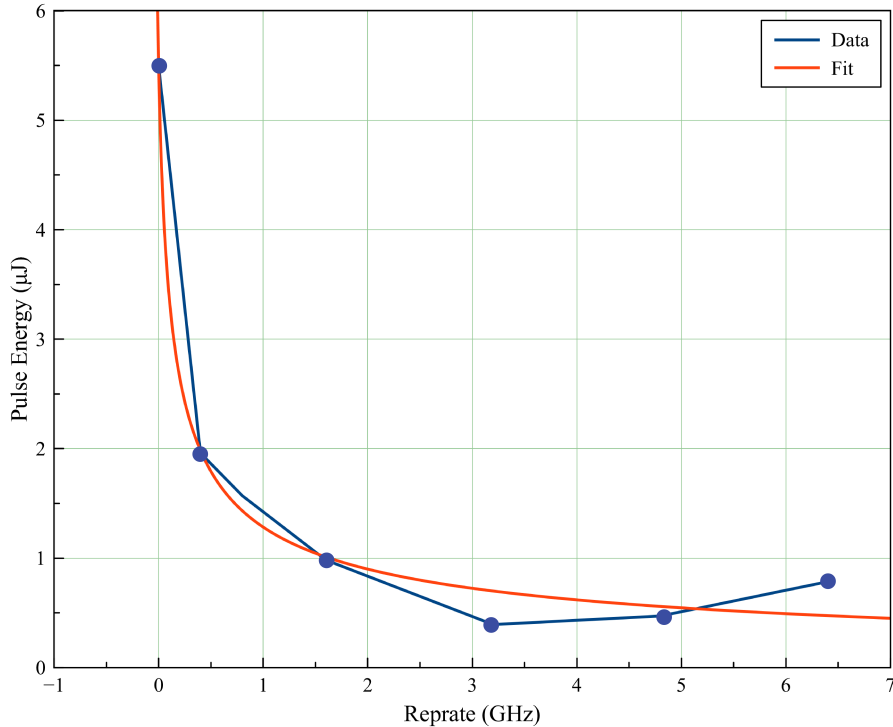


Figure 2.3: Calculated and simulated most efficient pulse energy for each pulse repetition rate.

2.4 Efficiency of Ablation

First, we solved the most efficient pulse energy for ablation analytically. We defined the efficiency as z_{abl}/ϕ where z_{abl} is ablation depth and ϕ is the pulse fluence. We assumed 1D material, similar to the TTM model. We also assumed ultra-short pulses, so any laser material interaction is instantaneous. For a single pulse, ablation depth is given by

$$z_{\text{abl}} = \delta \ln \frac{\phi}{\phi_{\text{th}}} \quad (2.10)$$

where δ is the penetration depth and ϕ_{th} is ablation threshold. This gives us the maximum efficiency pulse fluence as $e\phi_{\text{th}}$ where e is the Euler's number. More importantly, this gives the idea of a single pulse fluence that produces the maximum efficiency for ablation which can be extended to ablation cooled regime. The ablation efficiency for different repetition rates is simulated in Figure 6 where we can clearly see a peak for each repetition rate. This supports the idea of the best fluence for efficiency. Further, we can see the efficiency of a burst increases with repetition rate in Figure 2.4 which is plotted only for the most efficient pulse energies for each repetition rate.

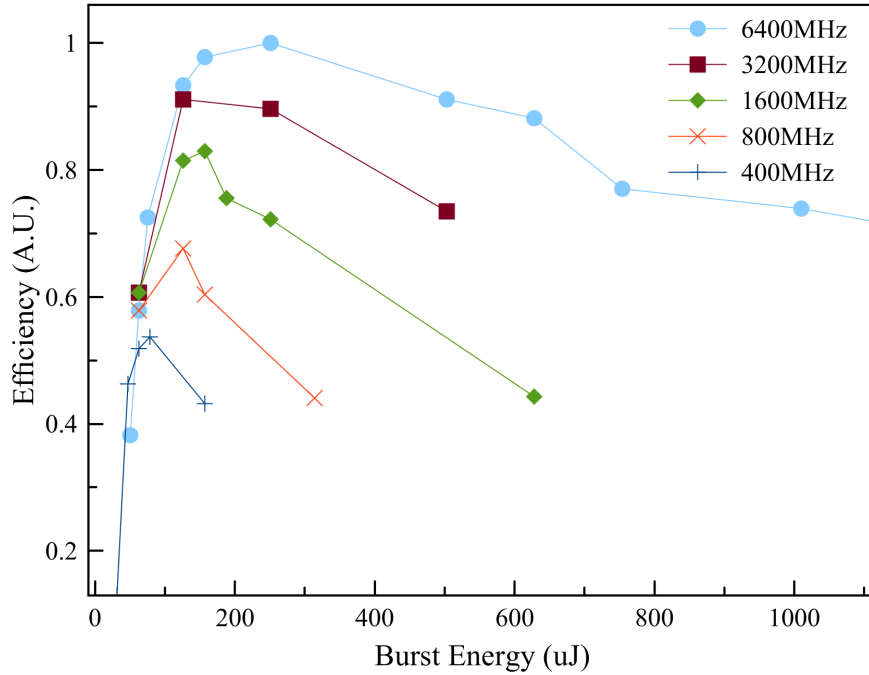


Figure 2.4: There is a peak of efficiency for each repetition rate. Also, the peak values for each of them increases for higher repetition rates. Efficiency values are normalized for maximum efficiency.

There is a peak efficiency we can find for each repetition rate. Disregarding any additional effects that are not included here, the burst energy should increase with repetition rate to achieve optimal ablation. It does not mean the ablated

volume decreases as we keep increasing burst energy. If you have excess power, one can still increase the ablated volume per burst. In practice, doing so would increase the heating on material which can cause collateral damage.

2.4.1 Tailoring Heat Distribution Inside the Material

Heat propagates from the surface of the material through the sample with equation

$$T(t) = \Delta T \sqrt{\frac{1}{1 + t/\tau_0}} + T_0 \quad (2.11)$$

where ΔT is the temperature difference between two points, T_0 is the initial temperature and τ_0 is the diffusion coefficient of the material. In Figure 2.5, temperature of the material after 20 ps from arrival of a single burst can be seen.

However, the temperature gradient after the burst does not give us the whole picture. To understand the dynamics of pulse-to-pulse interaction, we need to see how temperature gradient behaves during the processing. For example, in Figure 2.6, surface temperature and temperature 1 μm below the surface can be seen. The blue line represents the electron temperature of the surface. Temperature below the surface (green) stabilizes as pulses keep coming. It increases only after pulses stop coming, which supports the scaling of ablation with the number of pulses.

In Figure 2.7, only the repetition rate is changed from 1.6 GHz to 6.4 GHz. Apart from reaching a steady state more quickly, the subsurface temperature is significantly reduced. That is due to ablating the material faster and with more efficiency. Excess heat does not have time to diffuse inside the material. Again, only after the burst ends, subsurface temperature increases as surface temperature decrease.

It should be noted that the TTM model used here is a simplified version of

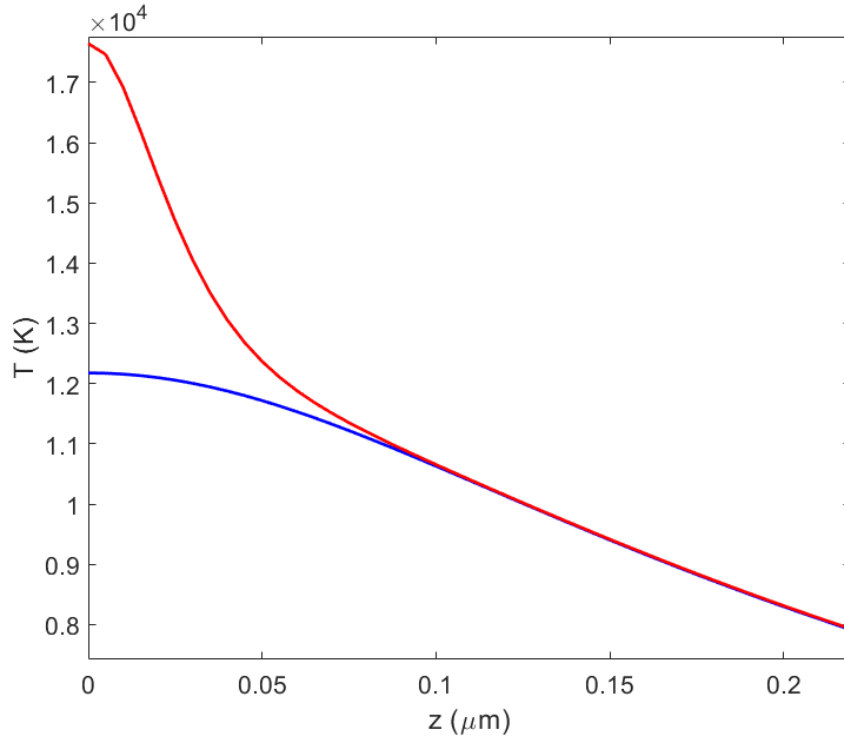


Figure 2.5: Surface temperature gradient before (blue) and after (red) 20 ps of a burst. Burst has 1.6 GHz pulse repetition rate with 160 pulses. Each pulse has 400 nJ energy.

the physics. Many effects such as plasma shielding are omitted from the model. The extent of the outcomes here should be studied in the future.

In the ideal temperature profile, the heat distribution from surface down to light penetration depth would be constant. If the temperature is high enough so that the next pulse can ablate all down to skin depth, then we would have maximum efficiency for pulses. Achieving and maintaining such temperature gradient is extremely complex. However, achieving a similar, smooth temperature gradient is easy by shaping the energies of pulses inside each burst. An example can be seen in Figure 2.8 where 3.2 GHz pulses with 590 nJ pulse energy.

This also agrees with my assumption of constant subsurface temperature experienced by each incoming pulse. The temperatures before any ablation (data point at the bottom) and after 2 pulses (data point at the top) are nearly the

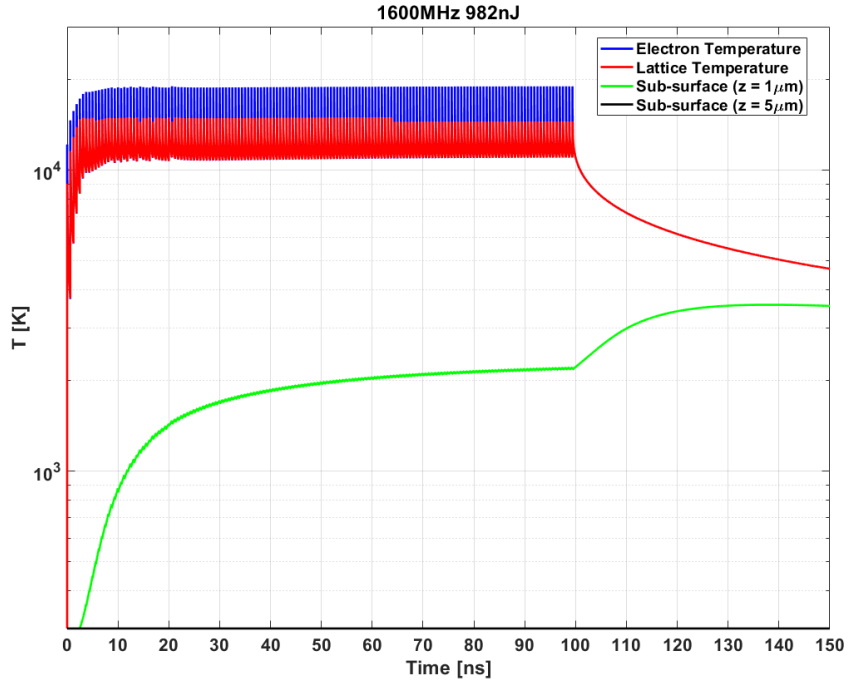


Figure 2.6: Temperature of surface (red), $1 \mu\text{m}$ below surface (green) and electrons at surface (blue). Pulse repetition rate is 1.6 GHz with 982 nJ pulses. Ablation only starts after lattice temperature reaches to 15000 K.

same. The temperature difference should vanish if we simulate for infinitely many pulses. The data points are chosen such that they are 20 nm below the surface.

The beauty of ablation cooled regime is keeping the material cool for very fast material processing. For a single repetition rate within the ablation cooled regime, the residual heat for different pulse energies is simulated. Residual heat is calculated as the sum of temperatures over the lattice since simulations assume 300K for room temperature which means the total heat of material before any pulse is 1.5×10^6 Kelvin. In Figure 2.9, we can see that as we increase the pulse energy, heating of the material also decreases. However, we are losing efficiency beyond 500 nJ (Fig. 2.4). Additionally, our simulations do not account for plasma shielding since we usually operate with pulse energies that don't produce a powerful plasma.

Then, the residual heat for different repetition rates is simulated and shown in

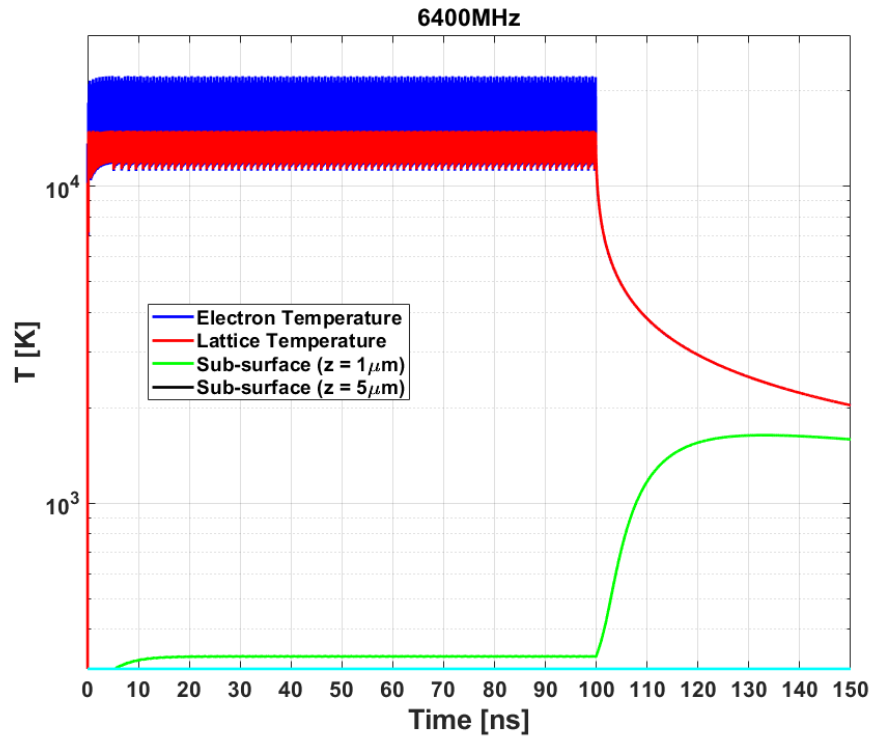


Figure 2.7: Simulation run for 6.4 GHz repetition rate pulses. Number of pulses is scaled to 640 to keep the burst duration same as other simulations. Subsurface temperatures are reduced significantly compared to 1.6 GHz case.

Figure 2.9. Some decrease of residual heat was expected since we are giving energy less time to diffuse into the material as we increase the repetition rate. Once again, the data point for 4.8 GHz case is simulated and added after predicting the curve which followed the fit closely.

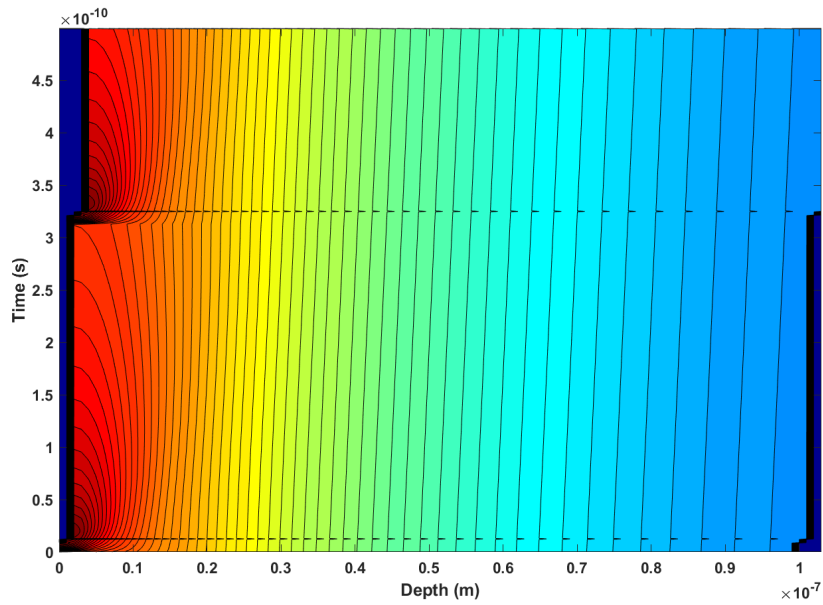


Figure 2.8: Contour of temperatures over 0.5 ns. The surface of the material is on the left side. After a pulse arrives, it ablated some of the material which resets the temperature to room temperature (300 K).

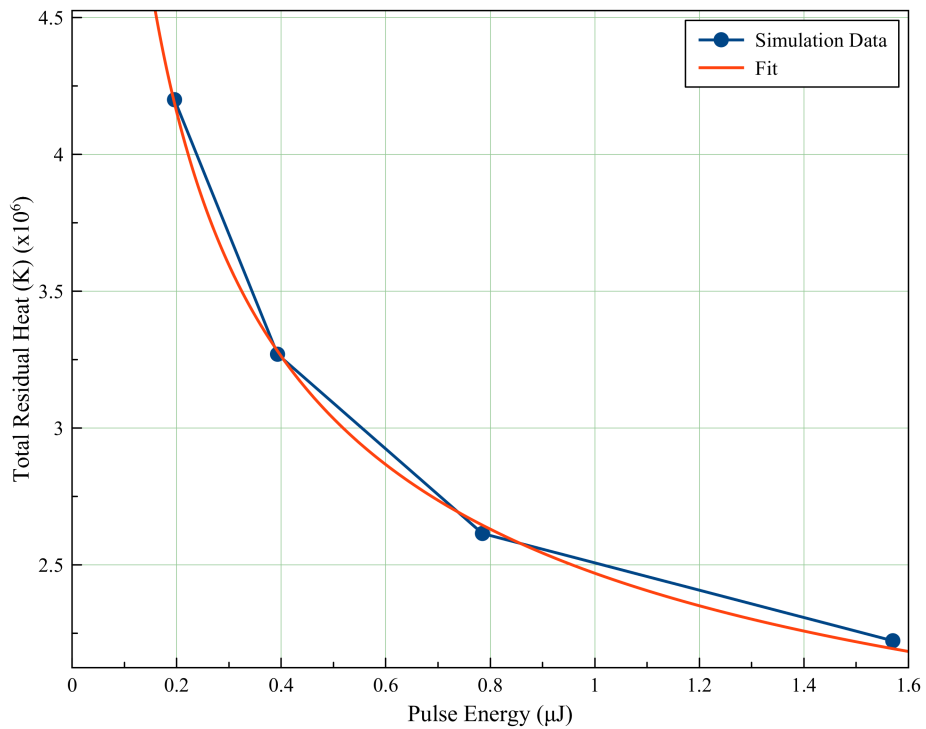


Figure 2.9: Residual heat after a single burst for different pulse energies. Repetition rate is 3.2 GHz.

Chapter 3

Experiments

Experiments were conducted to test and improve upon the simulation results using three different lasers on two materials. Then the results of the experiments were analyzed using a scanning electron microscope and laser scanning microscope.

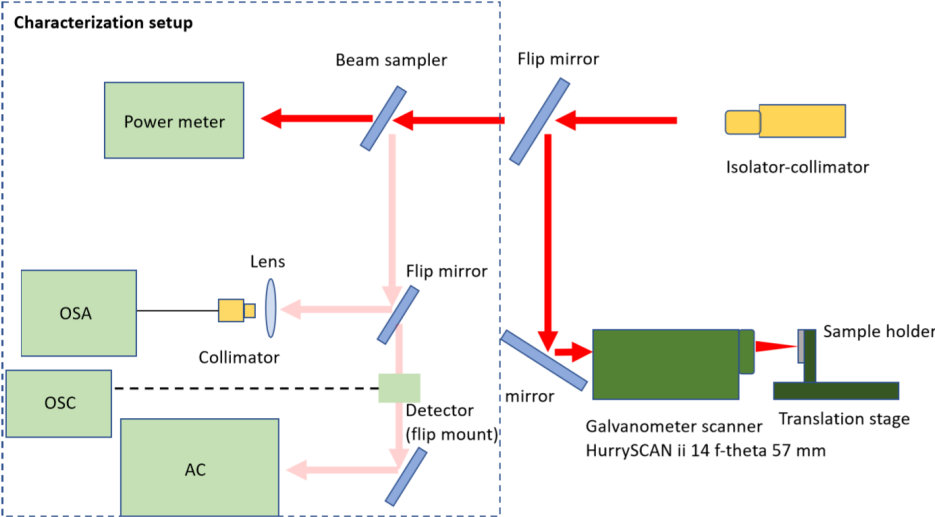


Figure 3.1: General setup for experimental laser systems.

All three lasers have their own processing and characterization setups. In Figure 3.1, common scheme of the lasers can be seen. A flip mirror is used to

switch between characterization setup and experiments. During the experiments, a beam blocker is moved manually in between processing to prevent excess exposure on samples. With characterization setup, average power, autocorrelation, and spectrum can be measured. The optical detector is necessary to observe the burst envelopes. Due to gain depletion [39] at burst mode operation, the gate that constructs bursts, usually an acousto-optic modulator(AOM), should be modulated to compensate. Details are explained in later this chapter.

3.1 Materials

There are two materials used extensively for the experiments for testing the simulation results and pushing the limits of ablation cooled material processing. First one is silicon which will let us set the basis for experiments. Second is human dentin to show a real-world biological application.

Silicon wafers are chosen for its low ablation threshold, flat surface and availability. Experiments are done on 10 Ω p-doped single side polished silicon wafers. The thickness is 500 μm for single burst experiments. 200 μm thick samples are used for drilling. The ablation threshold for the silicon is around 0.28 J/cm^2 for 1 μm wavelength with 400 fs pulse duration.

Human dentin is chosen for hard tissue experiments. It is quite a challenge to ablate the tissue without burning because of the composition and structure of the tissue. Dentin is mostly calcium and phosphate ions with about 30 % water. It has a porous structure which feeds the cells inside.

The samples we used were extracted teeth from patients at dentistry faculties of Hacettepe, Ankara and Erciyes Universities. Then, samples are diced using dicer with 1.5 mm thickness. All samples are kept inside water until experiments to preserve their optical properties. During the experiments, samples are frequently wetted with pipettes to prevent drying. Water is essential to preserve the structure and optical properties of the tissue.

Dentin is an important subject since any successful experiment on it can be easily translated to an application with minor additions such as a handheld probe. Laser ablation is already established in dentistry for both hard and soft tissue ablation. The most prominent issue is heating, forcing all current solutions to implement water jets with a probe to help with cooling the tissue. Proving ablation cooled material removal can ablate the tissue fast without any thermal damage can render lasers as invaluable tools for dentistry.

3.2 Laser Systems

Experiments are done in three distinct laser systems, referred to as 1.6 GHz, 1.46 GHz and 13 GHz from now on. The name refers to the repetition rate of pulses within each burst. For all of the systems, common parameters are used unless stated otherwise. In all three systems are Yb-doped fiber lasers with 1040 nm central wavelength. Bursts are repeated at 200 kHz except for some of the experiments which will be stated. Each system is explained extensively in Appendix A. High repetition rate between pulses is essential for the experiments. The main differences between the systems are given in Table 3.1.

	Pulse Duration	Spot Size
1.6 GHz	1-2 ps	23 μm
1.46 GHz	250-300 fs	11 μm
13 GHz	2-3 ps	23 μm

Table 3.1: The common parameters between laser systems is their central wavelength at 1035 nm. Also, they are all fiber based master oscillator power amplifier systems.

Another common property of these lasers is that they suffer from gain depletion. Otherwise, pulses within bursts have decreasing pulse energy as bursts proceed. That fails to ablate for pulses close to the end of the burst. The method explained in [40] is implemented for all three laser systems. All amplifier stages are modeled to find the rate of gain depletion for each burst duration and pulse energy. Then, input burst shape for each amplifier stage is calculated to get a

flat burst at the output. When the calculated envelope is applied to AOM, the effects of gain depletion is significantly suppressed.

GHz repetition rates were achieved by so-called repetition rate multiplier. It is a cascaded series of couplers with carefully adjusted fiber length, as seen in Figure 3.2. All couplers have 50% coupling ratio which divides the pulses into two equal parts. Then, the delay between each arm is tuned to have a half period of the current repetition rate at that stage. As a result, the repetition rate of the laser doubles at the output of next coupler. New segments of couplers can be added as long as the length of fibers is enough for splicing. At the last stage, one port is connected to the rest of the system while the other can be used for monitoring.

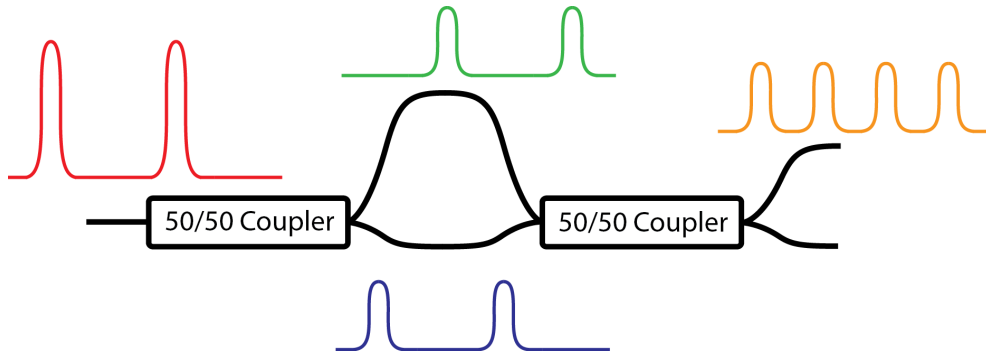


Figure 3.2: One stage of repetition rate multiplier. The length of the fibers are adjusted such that frequency of the pulse train doubles at each stage while the pulse energy is decreased by half.

Each set of experiment serves as a comparison between pulse energy, repetition rate and focusing optics. The details of the experiments are given below.

3.2.1 1.6 GHz experiments

The first set of experiments were done with a non-PM laser where the pulse repetition rate is 1.6 GHz, and the burst repetition rate is 100-200 kHz. The scanning speed of the galvo scanner is kept at maximum to be able to apply a single burst on a single point. This way, we can measure the ablated volume per burst. 56 mm focusing lens is mounted on the galvo scanner.

The scaling of ablation cooled regime is mostly tested with this laser, on silicon. Pulse energies from 50 to 120 nJ are applied on silicon. The number of pulses is varied between 200 to 1800 per burst which translates to 125 ns to 1.25 μ s.

An alignment pattern encircling the experimenting area is applied repeatedly to find the focus and fix any tilt on the sample. Then, two simple shapes (usually square) separated by a few millimeters are applied at once. This is due to a technical limitation of the galvo scanner we use. The jumping speed can be as much as 6 m/s compared to drawing speed of 2 m/s. Since at least 4 m/s is required to differentiate between each burst, the holes created by jumping from one pattern to the other is used.

3.2.2 1.46 GHz experiments

The second system used for the experiments had another Yb doped MOPA laser. However, this time, all fibers are polarization maintaining. As a result, losses at the grating compressor is not as high as before. This lets us reduce the power requirements of the laser. Additionally, a commercial OCT (Thorlabs CALLISTO) is integrated with the output for both imaging and scanning purposes. The focusing lens (LSM02-BB) can focus the beam down to 11 μ m, decreasing the power requirements by a factor of 4.3 times. Further, the pulse duration for 25 nJ pulses can be compressed down to 270 fs, contributing the peak power even more.

This system is mainly used for dentin experiments. The parameters explained above all let us decrease the average power while utilizing more of the pulses for ablation which reduces the average power we have to apply on the tissue. This way, we can reduce the heating without sacrificing ablation.

Single burst ablation and drilling experiment were done on both silicon and dentin. Similar to 1.6 GHz experiments, the scanning speed is kept at maximum to differentiate the effect of each burst. For drilling experiments, scanning speeds of 0.25, 0.5 and 1 m/s are tested. Raster scanning and concentric circles with reducing diameters are applied on samples for single burst and drilling

experiments.

3.2.3 13 GHz experiments

For the last set of experiments, I used a 13 GHz laser coupled with another galvo scanner. The galvo scanner lens is the same one as 1.6 GHz systems which has 56 mm focal distance which can focus down to 23 μm . The burst repetition rate is set to 200 kHz.

With this system, I can observe the effects of much higher repetition rates compared to our previous experiments. The simulations suggest the pulse energies required for ablation will drop significantly while the number of pulses necessary within a burst to achieve ablation will increase.

The experiments can be grouped into 3 categories: single burst, repeated lines, and drilling of silicon.

Before starting each experiment, similar to previous setups, an alignment pattern is applied to the galvo scanner. The pattern is a square that defines the working area and lets us adjust the sample surface perpendicular to beam propagation. In single burst experiments, the pattern is virtually the same as 1.6 GHz experiments. As for the drilling experiments, 5 concentric circles with 20 μm between each other is applied 10 times on 200 μm silicon wafer. This is done to avoid blocking beam with the wafer as drilling continued and prevent sticking due to melted parts. Finally, a slow, linear pattern is applied 1, 2, 5 and 10 times to quantify drilled volume.

As the repetition rate between pulses is increased more, the required pulse energy also decreased, as simulations suggested. Now, pulses as low as 10 nJ can ablate silicon consistently. When the regular ablation threshold of silicon for 1 μm is considered, which is around 1 μJ for my pulse duration and beam size, the results are significant.

3.3 Analysis

Two main methods of analysis were scanning electron microscope (SEM) imaging and laser scanning microscope (LSM) measurements.

Scanning electron microscope (SEM) is widely used for imaging for its high resolution. FEI Quanta 200 F, which has 3 nm resolution at 1kV, is used. The SEM used can achieve 1 nm resolution. The images will provide quality assessment for ablation quality and collateral damage. The working principle of SEM is through collecting secondary electron generated on the surface due to excitation from a highly focused electron gun. The generated electrons are gathered to a target via a positively charged conductive mesh where a detector lies inside.

Silicon samples didn't require any preparation for SEM since it is a semiconductor. A piece of conductive tape is used to connect the top surface and the stub as a channel to prevent electron accumulation.

Dentin samples needed conductive coating beforehand. 10 nm of Au/Pd alloy is coated using RF sputtering. After coating, a channel between surface and stub is created with conductive tape since the samples are thick.

LSM can provide depth information with great accuracy. I used VK-X 100 from Keyence for the measurements. So, the vertical resolution is documented to be 10 nm while the horizontal resolution is 50 nm. I used it to measure the ablation depths of processed samples. The optical microscope embedded to the device can take color images which lets us evaluate the quality and damage of the processing further.

The processed sample does not require any preparation before measurement. They can be used or analyzed after the analysis.

Chapter 4

Results & Discussion

In this chapter, the results of the experiments done on silicon and dentin are presented. The results are gathered with all three laser systems.

4.1 Verification of Simulation Claims on Silicon

4.1.1 1.6 GHz Results

There were two sets of experiments on silicon using 1.6 GHz system. First one is scaling of ablation with the number of pulses. Second is drilling 200 μm silicon wafer using the best parameters from the first experiment.

In figure 4.8, single bursts with a changing number of pulses are presented. Bursts with lower than 200 pulses fail to ablate consistently, so those results are discarded. The quality of edges in terms of melting increases until around 1000 pulses. After that, heating starts to overwhelm ablated parts. If we extend the number of pulses even further, melted silicon starts to pour into the ablated cavity.

The melted region around the cavity doesn't increase as the number of pulses is increased. This suggests any heat-induced to the silicon by a pulse is carried away by the next incoming one. The heat deposited on the material is defined by the repetition rate and pulse energy when in ablation cooled regime, not by the total energy of the burst. Hence, proving the first claim by toy model, removal of heat induced by a pulse by the next incoming one.

SEM images led us to the main limitations of this laser which are peak power and peak intensity. The diameter of the cavity continued to increase which is shown in Figure 4.2a. However, the depth of the cavity seems to stop increasing from LSM measurement in Figure 4.2b.

That does not mean the ablation stops after 1000 pulses. In reality, ablation continues to occur, but due to insufficient peak intensities of edges of the beam, melting overwhelms ablation. Melted materials pour into the drilled hole, which decreases the depth of it in measurements.

The results mentioned above confirm the TTM simulations. The depth of the drilled holes increased linearly, even though a low number of pulses fails to ablate. Also, the energies we use are well below the ablation threshold of silicon for a single pulse. Therefore proving the second claim, linear scaling of ablation depth with the number of pulses.

4.1.2 1.46 GHz results

The power scaling of ablation cooled regime is proven in the previous set of experiments. Here, those outcomes are pushed even further, mainly to decrease heating.

In Figure 4.3, the quality of ablation can be seen. Melted crater walls are still there but reduced compared to 1.6 GHz case even though we were using smaller pulse energies. Usually, reducing the pulse energy or increasing the burst duration result with more heat. The improvement, in this case, can be attributed

to shorter pulse duration but mostly due to the smaller spot size.

The pulse energies presented here are not the lowest or the best. They can be further improved with optimizing the optics. However, that is beyond the scope of this thesis. Another direction to go would be to increase the spot size while also increasing the pulse energy, as opposed to what is presented in this section. This way, the ablation threshold in terms of pulse energy would be increased, but the threshold for fluence would stay the same. As a result, 1D approximation of heat diffusion will come closer in practice, heating the material less with higher ablation efficiency and speed.

4.1.3 13 GHz results

With 13 GHz pulse to pulse repetition rate, nearly an order of magnitude reduction at pulse energy for ablation is expected. In Figure 4.5, SEM images of single burst experiments are shown. Pulse energy is adjusted from 10 nJ to 80 nJ for constant burst energy.

Here, it is clear that increasing the pulse energy is not beneficial at all. After 25 nJ, heating was so dominant that it melted more area than it ablated. Though, this is mostly due to the Gaussian nature of the beam. Best results were gathered using 15 nJ pulses with this laser where ablation is consistent, and melting is not so prominent. Finally, experiments done with 5 nJ can be seen in Figure 4.6 with the same burst energies to cases shown above.

5 nJ fails to achieve any ablation, as seen from LSM measurements. Peaks due to heating, peaks of silicon are formed on the surface. It still should be possible to achieve ablation with 5 nJ pulses. It did not fail to ablate due to low pulse energy, but because the repetition rate was not enough to support high enough surface temperature for 5 nJ. TTM simulations suggest that if the repetition rate is increased, 5 nJ pulses will be able to ablate silicon with current pulse duration and spot size.

Generally, ablated depth scales with pulse energy. In ablation cooled regime, we expect it to scale also with the number of pulses from the simulations. LSM measurement in Figure 4.7a support that. The maximum power of the laser limits the burst durations for higher pulse energies. A more interesting take is to calculate the efficiency of ablation. After scaling for total energy applied per unit area, in Figure 4.7b, 15 nJ case beats both higher and lower energies in terms of efficiency.

Since 15 nJ pulses produced the best results, the same pulse energy is used for drilling. In Figure 4.8, SEM images of experiments on 200 μm thick silicon are presented. Scanning speed is adjusted such that spots in succession barely touch each other. Each sample is scanned separately for changing the number of passes.

1 pass and 2 pass cases were not able to cut through the silicon wafer. However, 5 pass case managed to ablate through the wafer, even though it was not consistent. The melting inside the drilled line can be seen in Figure 4.8c. At 10 passes, a disc is separated from the rest.

This concludes the proof of the third claim which is being able to lower the ablation threshold by increasing the number of pulses as long as the pulse-to-pulse repetition rate is comparable or more than the thermal relaxation of the processed material. The ablation threshold has been lowered another 10 times compared to previous results in [17] for silicon while reducing the burst energy.

4.2 Ultrafast ablation of Dentin Suitable for Real World Applications

Results from 1.6 GHz and 13 GHz systems are omitted. Experiments done with that laser failed to ablate the dentin before moving on to 1.46 GHz system. The pulse duration and focusing of 1.46 GHz proved to be better suited for tissue ablation. It might be possible to achieve ablation without carbonization after

optimizing the parameters of the laser and scanning, but it is not tested further.

4.2.1 1.46 GHz results

The best results for this experiment were achieved using 25 nJ pulses with 730 pulses per burst (500 ns burst duration). After fine alignment using OCT, we managed to ablate the tissue without any heat damage.

The ablated volume here is $1.4 \times 10^{-3} \text{mm}^3$ with 2 m/s scanning speed. So, the ablation rate here is $0.28 \text{mm}^3/\text{s}$. That is over 6 times faster compared to our previous drilling speeds [33].

The cracks visible on the sample in Figure 4.9 are not due to ablation. They can be found all over the surface likely formed while dicing process. The depth of the hole is $20 \mu\text{m}$. In Figure 4.10, in-depth analysis of another sample is presented. Similar to Figure 4.9, there is no thermal damage, but it failed to ablate all of the processed areas.

4.3 Discussion

There are a few obvious steps to progress this work further. First, using some beam shaping which will decrease residual heat on the sample with appropriate focusing optics. Required pulse energy may increase depending on the chosen lens, but few tens of nJ are still quite easy to achieve.

Second, a laser designed with considering low pulse energies and high average powers. All three lasers used here were designed to produce much higher pulse energies for experimentation purposes. Such a design will be less complex while let us achieve shorter pulse durations.

Similarly, burst repetition rates here were restricted to 200 kHz by amplified

spontaneous emission of lasers. In most cases, instead of sending more bursts, increasing the number of pulses inside a burst is more desirable. Burst repetition rates around a few kHz would help to keep the average power low without sacrificing anything other than ablation speed. Even then, by merely adding more pulses, ablated volume per burst can be increased.

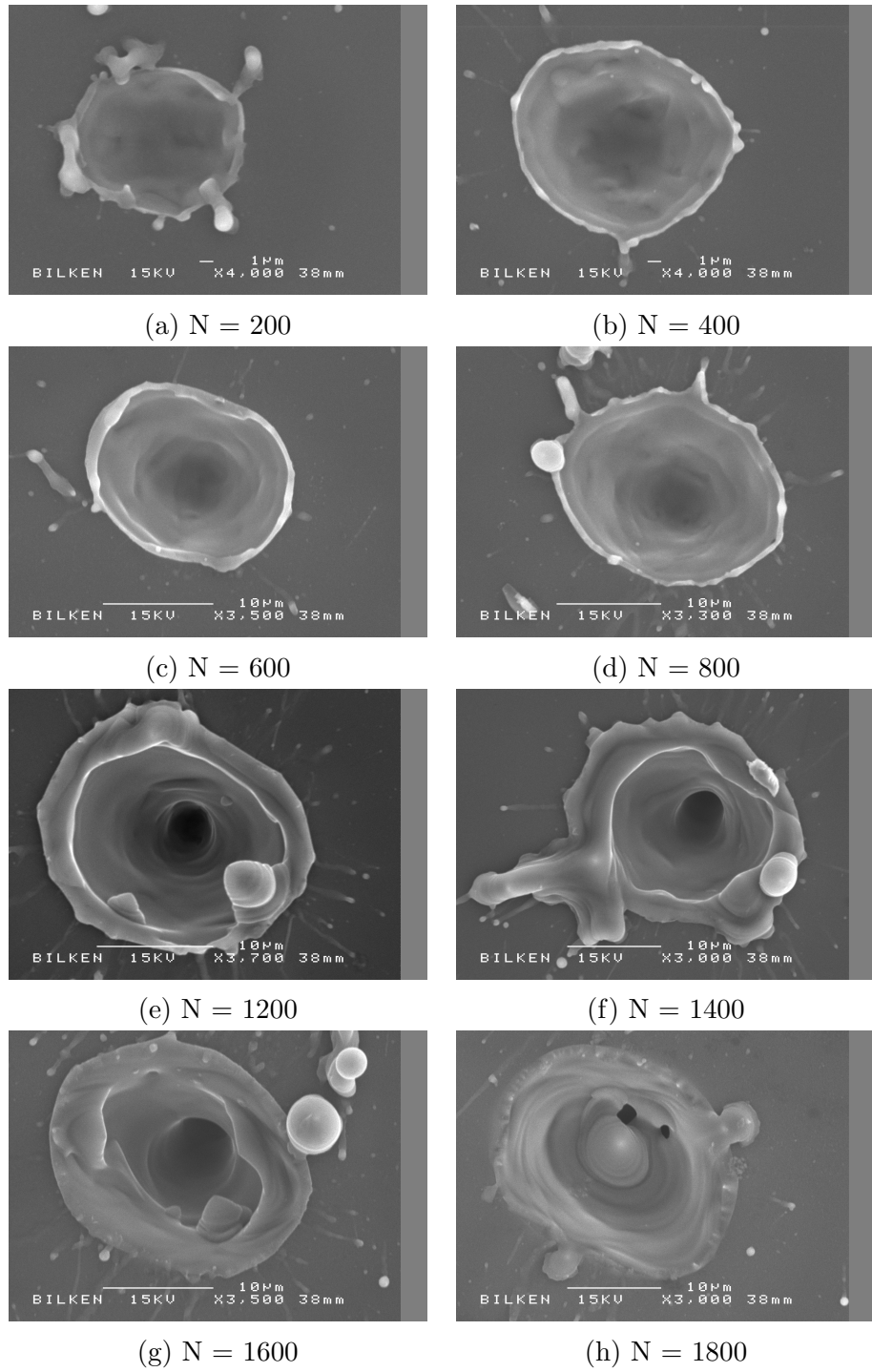
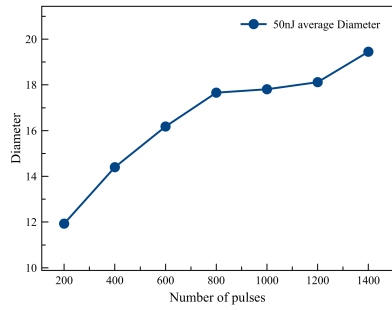
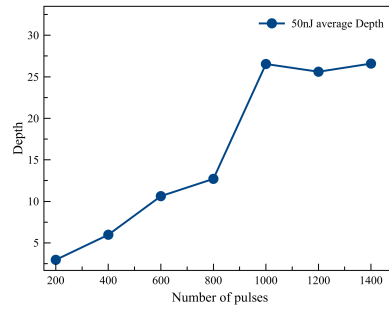


Figure 4.1: SEM images of silicon samples. Each was processed with a single burst containing a various number of pulses per burst. Pulse energy is kept constant at 50 nJ



(a) Average diameter of ablation for bursts with 50 nJ



(b) Average depth of ablation for bursts with 50 nJ

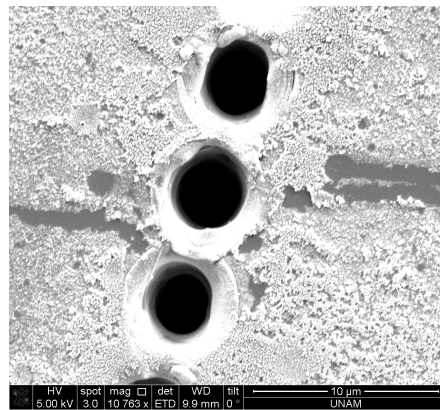
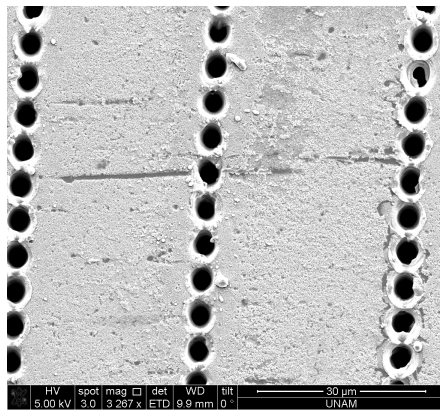


Figure 4.3: SEM images of silicon experiment. One burst per spot with 25 nJ pulse energy, 730 pulses

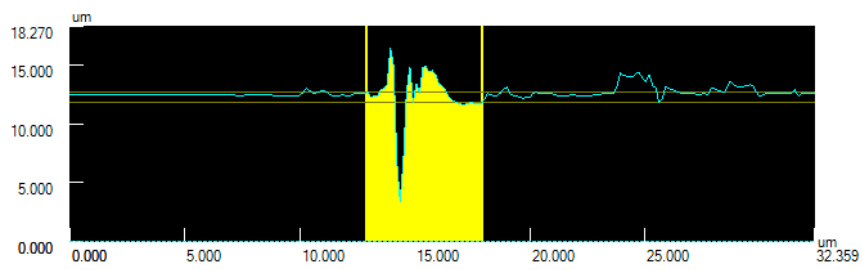
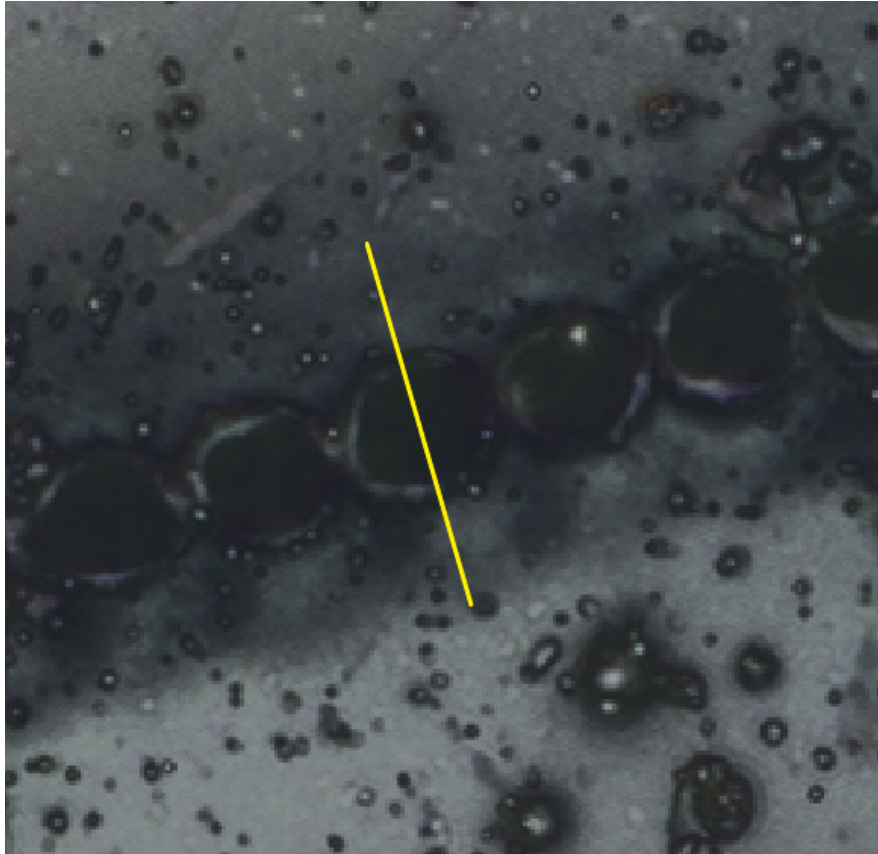
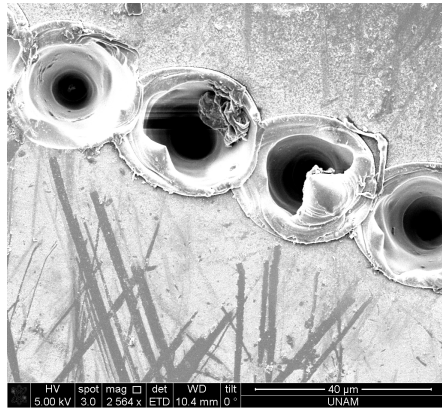
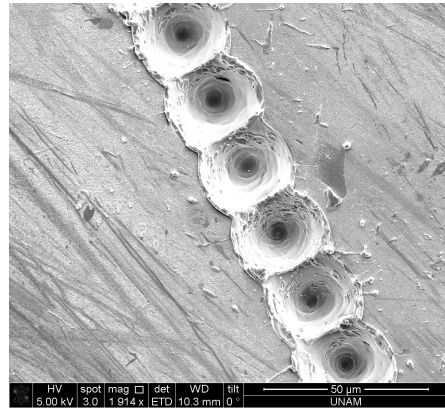


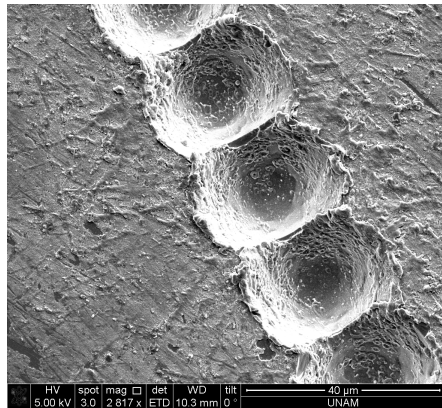
Figure 4.4: LSM image of one burst per spot with 25 nJ pulse energy, 730 pulses. The depth of the holes are measured as 9 μm while the diameter is 5 μm .



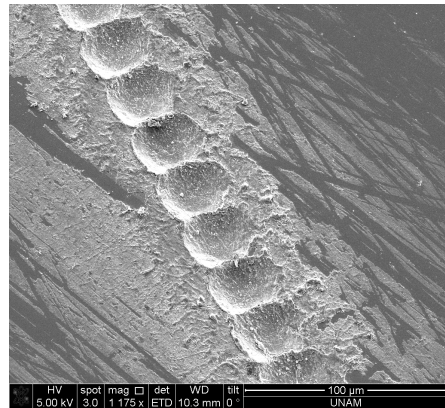
(a) 10 nJ pulses



(b) 15 nJ pulses



(c) 25 nJ pulses



(d) 80 nJ pulses

Figure 4.5: SEM images for $160 \mu\text{J}$ burst energy with 10-80 nJ pulse energies. Number of pulses per burst are adjusted to keep the burst energy constant.

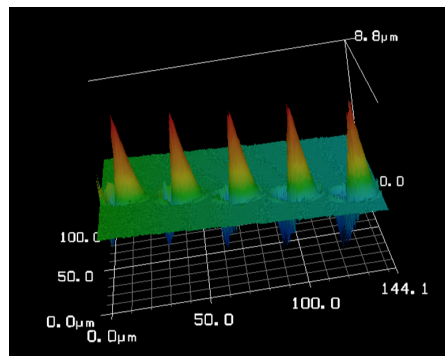
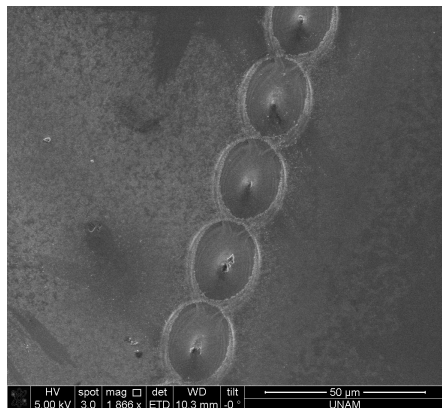
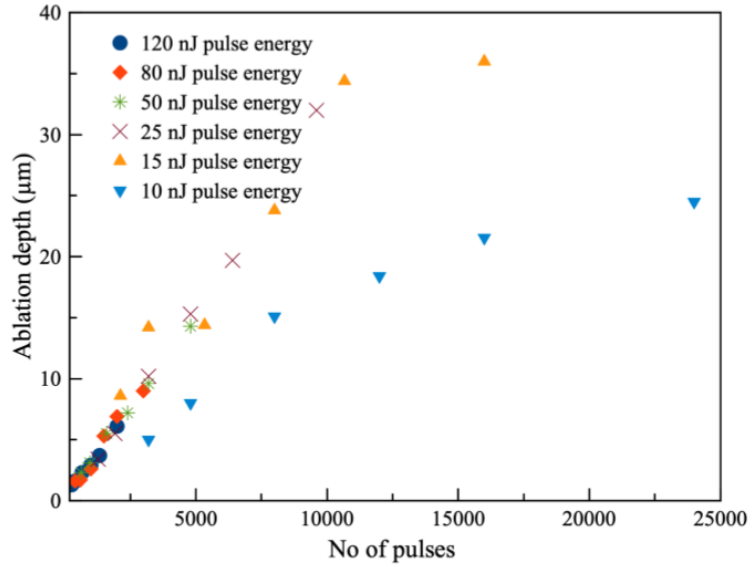
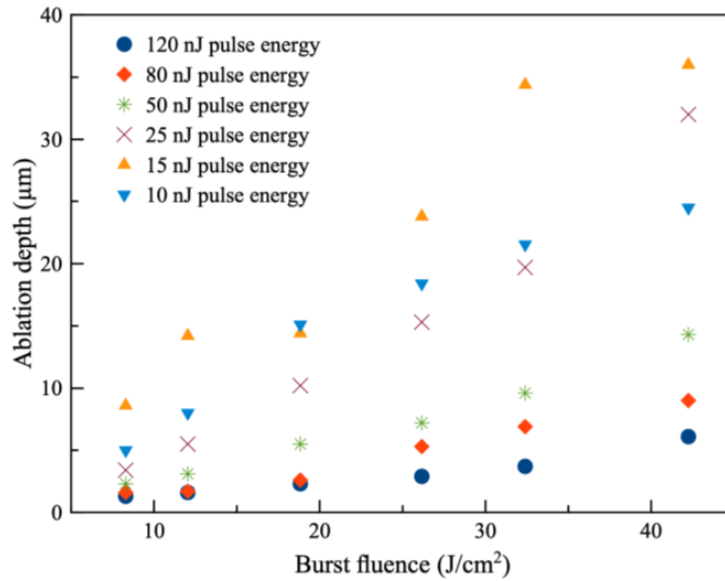


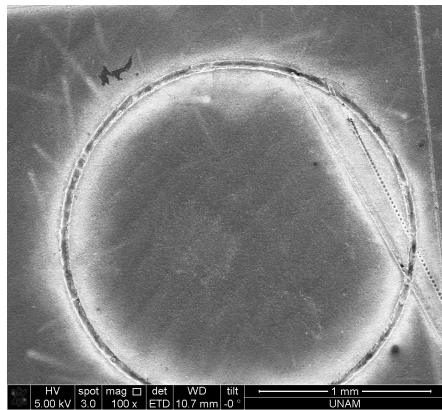
Figure 4.6: SEM image and LSM measurement of silicon processed with bursts containing 24000 pulses with 5 nJ energy each.



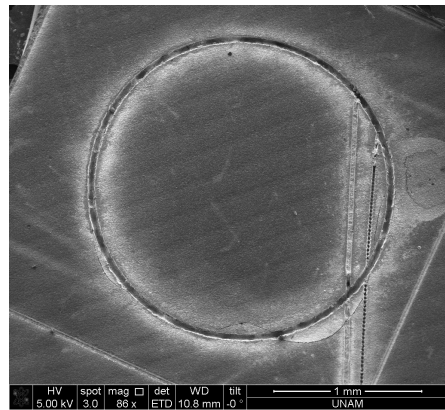
(a) Scaling of ablation depth with burst duration for different pulse energies. Longer burst duration are only supported for lower pulse energies due to power constraints.



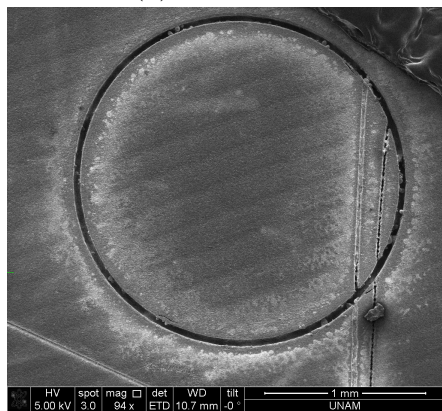
(b) Efficiency of ablation when adjusted for total fluence. As predicted from simulations, there is an ideal pulse energy for certain material and pulse repetition rate. For 13 GHz on silicon, that pulse energy is 15 nJ.



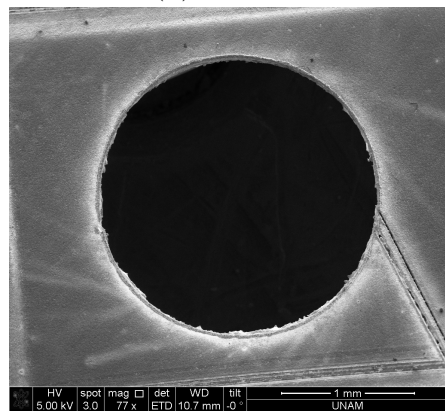
(a) Single pass



(b) 2 passes

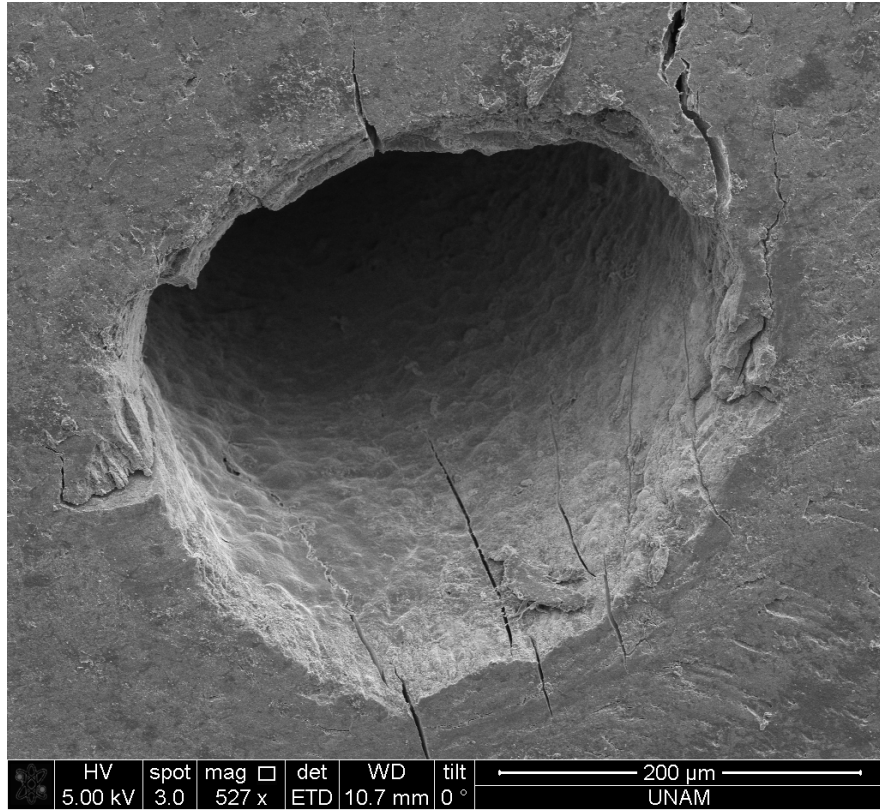


(c) 5 passes

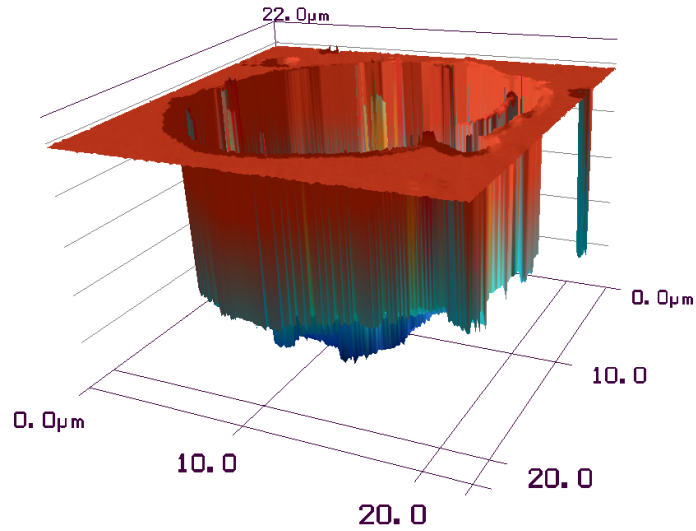


(d) 10 passes

Figure 4.8: Drilling 200 μm thick silicon with 15 nJ pulses. Each burst consists of 6000 pulses. Scanning speed is constant at 2 m/s. 1, 2, 5 and 10 passes are applied on different samples. SEM images for them are (a), (b), (c) and (d) respectively.



(a) SEM image



(b) LSM measurement

Figure 4.9: Ablation of dentin with 25 nJ pulses, 730 pulse per burst. Helix pattern is applied with 4 mm diameter shown in (a). Only the center of the pattern achieved ablation. Rest of the tissue remained untouched. The depth of the hole is measured to be 20.0 μm from LSM measurement in (b).

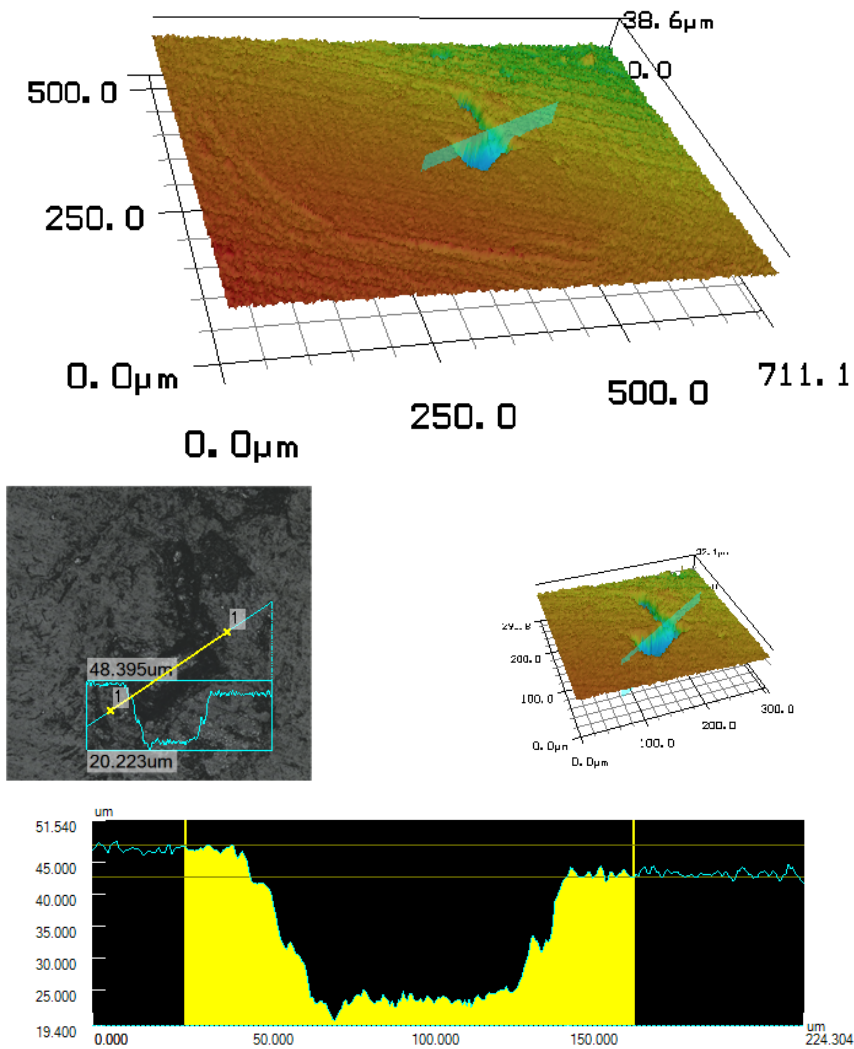


Figure 4.10: Another dentin sample 25 nJ pulses, 730 pulse per burst. Same helix pattern is applied with 4 mm diameter. Center of the pattern as well as a line were ablated without any thermal damage. Bottom surface of the sample stays flat, supporting our deduction of ablation without heating.

Chapter 5

Approaching from Broader Perspective

In this chapter, the topics studied along with the thesis are presented. Subjects are not unrelated, but they aren't within the main idea of the thesis necessarily.

First, novel laser oscillator ideas are surveyed for material processing. The motivation was to design a laser that accompanies the results presented in this thesis. Low energy pulses with GHz repetition rates produce better ablation efficiency and speed. Hence, thin disk lasers were a great candidate. Producing pulses with high energy directly from oscillators is proven to easily achievable. Although the repetition rates are usually at the MHz range, it is shown that repetition rate multipliers can be used to achieve GHz levels. A working simulation model of dissipative soliton and similariton are presented with record pulse energies.

Then, producing high-density 3D computer generated holograms from a single layer diffractive optical element is shown. The method taps into a connection between Fresnel and Fourier holography, incorporates Fresnel zone plates, diffrusers, and the kinoform principle, used together to generate a single hologram that projects 3D dynamic images with low crosstalk. This method can allow extremely fast additive material processing such as 3D printing, in contrast to

what has been presented so far, namely ablation which is essentially a subtractive process. We experimentally showcase this new capability with 3D dynamic display prototypes. These results are still far from fundamental limits imposed by physical optics; we show that the quality and number of planes scale up linearly with the number of hologram pixels. Finally, we demonstrate 3D projection of a complex object, namely, a model spacecraft, that can be viewed over the entire 4π solid angle.

5.1 Adapting Mode-locking Regimes to Thin Disk Lasers

Dramatically lowering the pulse energies required for ablation urged us to explore new laser designs. Even though ablation cooled regime needs repetition rates comparable to relaxation times, the laser itself can produce pulses at lower repetition rates out of the box as long as pulse energies are increased proportionally. In fact, lasers used in experiments included in this thesis always used "repetition rate multipliers" to generate GHz repetition rates from 100 MHz or lower pulse trains, as explained in Chapter 3. This led us to thin disk lasers (TDL) where tens of μJ pulse energies can be produced with ease [41]. Later, repetition rate can be increased in exchange for pulse energy similarly. Producing high energy pulses directly from oscillator has many advantages such as reduced complexity, cost and increased stability of laser.

So far, only soliton mode-locking [42] and Kerr lens mode-locking [43] has been demonstrated with higher pulse energies in TDLs. Both mode-locking regimes restrict the achievable pulse energies due to their susceptibility to nonlinear phase shifts [44]. Other mode-locking regimes such as chirped pulse oscillator are still only proof-of-principle with very low output pulse energies [45]. Even in the TDL with record pulse energy of 80 nJ [46], nonlinear phase shifts are kept below π due to incompatibility of saturable absorbers with the power level. The incentive to keep pushing for higher repetition rate oscillators still exist, but the

best published result is for 260 MHz [47] with 0.3 μJ pulse energy without self starting. So, we decided to keep pushing for the pulse energy instead of higher repetition rates. Here, dissipative soliton [48] and similariton [49] mode-locking regimes are proposed to be adapted to TDL. Both regimes can withstand much more nonlinear phase shifts (10π). Additionally, pulse durations in soliton mode-locking is always close to transform limited which also produces more nonlinear phase shifts due to high peak powers. Both properties mentioned contribute to reaching much higher pulse energies with dissipative soliton and similariton mode-locking regimes.

We designed oscillators where pulses experience a single optical effect (gain, loss, dispersion or nonlinearity) inside a segment, hence we named them discrete similariton and discrete dissipative soliton [50]. We used easily achievable parameters while designing the lasers. Thin disk gain is kept at 1 dB per reflection. The modulation depth of SESAM is 5%.

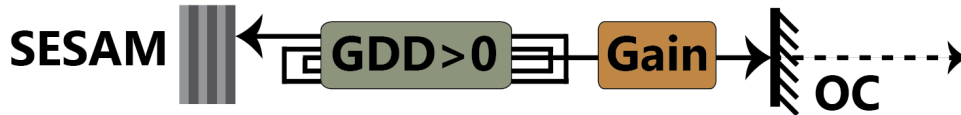


Figure 5.1: Passive Multipass cavity for discrete dissipative soliton adapted for TDL

Dissipative soliton is designed around passive multipass cavity where pulse experiences dispersion and nonlinearity consecutively multiple times before hitting the thin disk to be amplified (Figure 5.1). The output coupler is chosen as 10%.

Phase space is shown in Figure 5.2. The horizontal axis indicates how far the pulse is from transform limited case while the vertical axis is the spectral width. The color corresponds to the relative pulse energy. A “staircase like” propagation of the pulse through phase space can be clearly seen. Pulse experiences a single optical effect inside each segment since all other effects are negligible. DCM acts as a dispersive medium, air has the most powerful contribution to nonlinear phase shifts and thin disk only amplifies the pulse with respect to its bandwidth. Output pulse energy is 200uJ with 17 ps pulse duration and 10 nm spectral width.

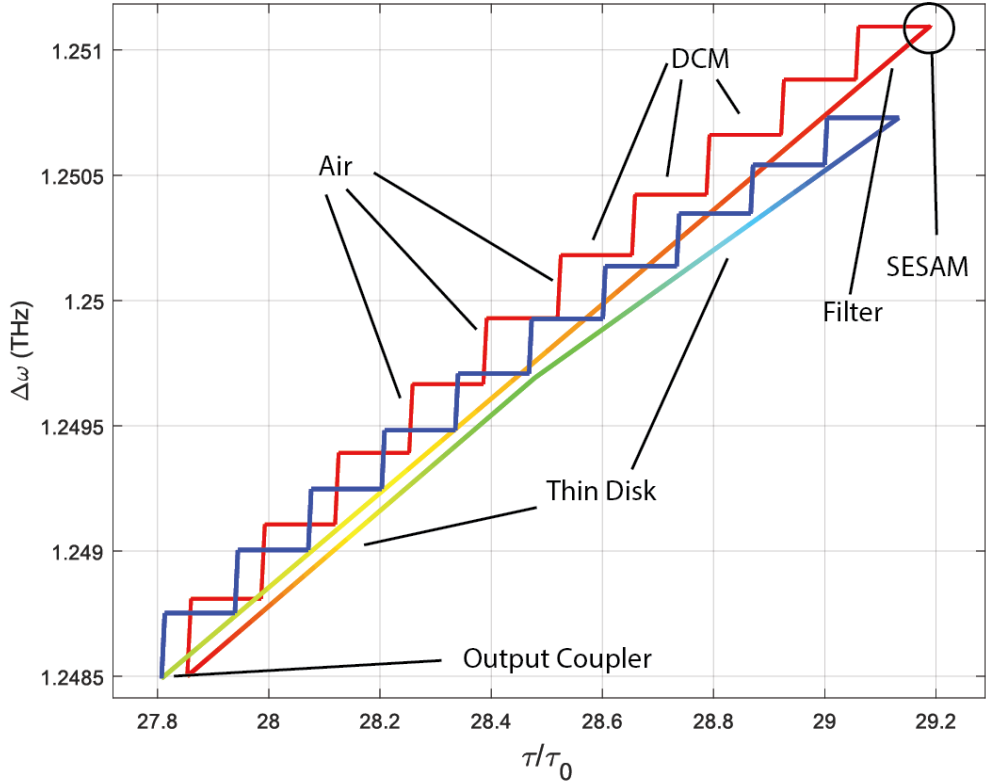


Figure 5.2: Phase space of a single roundtrip around passive multipass cavity after the pulse stabilizes.

In Figure 5.3, the compressed output and its spectrum can be seen. The pulse energy at the output is $200 \mu\text{J}$ with 10 nm spectral width. 17 ps pulses are compressed down to 374 fs .

Another approach to utilize nonlinear effects would be similariton mode-locking where both spectral and temporal shape of the pulse are parabolic. Similariton implies high loss for pulse to go back to the state it started in the cavity, therefore requires higher gain from the laser which in turn necessitates an active multi-pass cavity design (AMC). In AMC, pulse goes through gain and dispersive medium multiple times at each roundtrip (Figure 5.4). This way, pulse experiences significant gain which in turn allows for output coupler as high as 50% without losing mode-locking.

Resulting mode-locking regime is plotted on a phase space (Figure 5.5). Similar

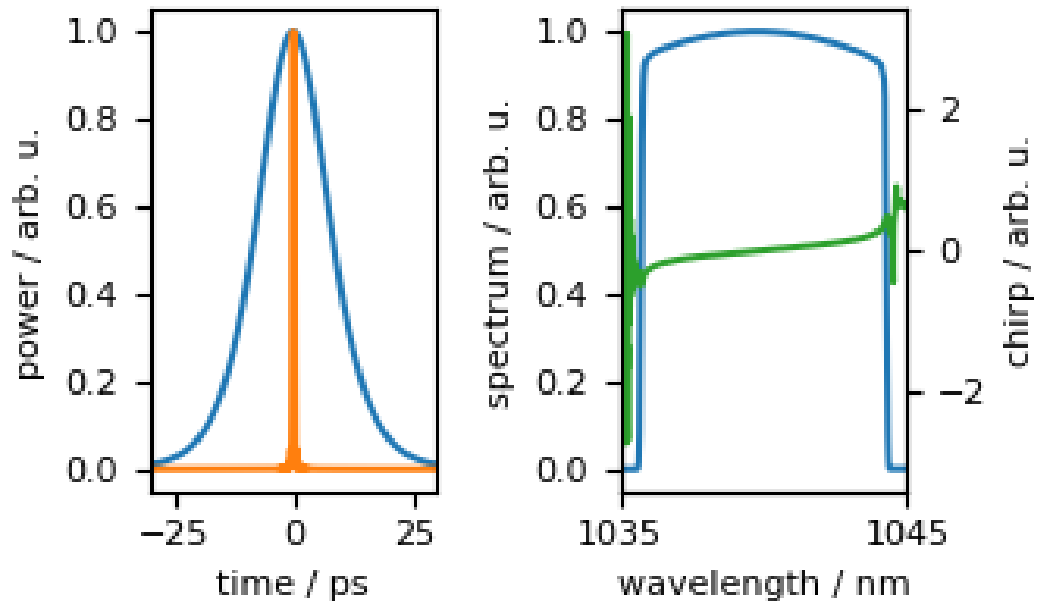


Figure 5.3: Dissipative soliton TDL: temporal (left) and spectral (right) shape of pulses extracted at the position in the resonator where the spectrum is broadest. The numerically dechirped and nearly transform-limited pulse is indicated in orange color. The chirp of the spectrum is indicated in green. The spectral shape obtained is characteristic for the all-normal dispersion regime. Figure taken from [50]

to dissipative soliton laser, we can see the discrete nature of the laser from phase space.

Output pulse energy is 950uJ with 5 ps pulse duration and 40 nm spectral width (Figure 5.6). After compression, pulse duration drops to 95 fs.

There are three significant outcomes to these simulations. First, contrary to common belief, optical effects required for similariton and dissipative soliton mode-locking don't have to act simultaneously. They can act in turns to support the pulse, hence the discretization. Second, this is the first time, best to our knowledge, air is exploited for its nonlinear effects for a mode-locked oscillator. Finally, we showed mode-locking regimes that were common and extremely beneficial in fiber lasers can be adapted for TDLs increased the output pulse energy by more

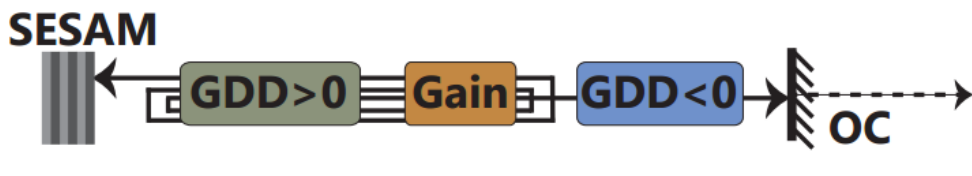


Figure 5.4: Active multipass cavity for discrete similariton laser adapted to TDL.

than an order of magnitude straight from the oscillator.

The next step would be to implement either dissipative soliton or similariton laser. Then, a repetition rate multiplier should be adapted from fibers to TDL in order to use them for ablation cooled material processing. Regardless of this use case, pulse energies in the order of hundreds of microjoules from an oscillator is a significant improvement over current technologies.

5.2 3D Projection from Single Hologram Layer

So far, only subtractive methods are explored, namely ablation. Another option for material processing is additive methods, commonly used for 3D printing applications. Traditionally, high fluence is required to activate the photoresist, which necessitated sharp focusing, similar to ultrafast ablation. Holograms can replace lenses for focusing or even construct any arbitrary image which can speed up the printing significantly [51]. Volumetric holograms can increase the speed even further by printing a 3D object with single exposure.

The Computer generated holograms (CGHs) are ideally suited for use with further potential as new holographic media are emerging [52]. However, the problem of how to project truly 3D images with full depth control using CGHs remains open. Fourier holograms can provide high-quality images but they have to be created at the focal point of a lens, which restricts the projection space to few centimeters [53]. On the other hand, Fresnel holograms can project images over a substantial portion of space yet, there are no methods to create images with high resolution and they are limited to few planes [54].

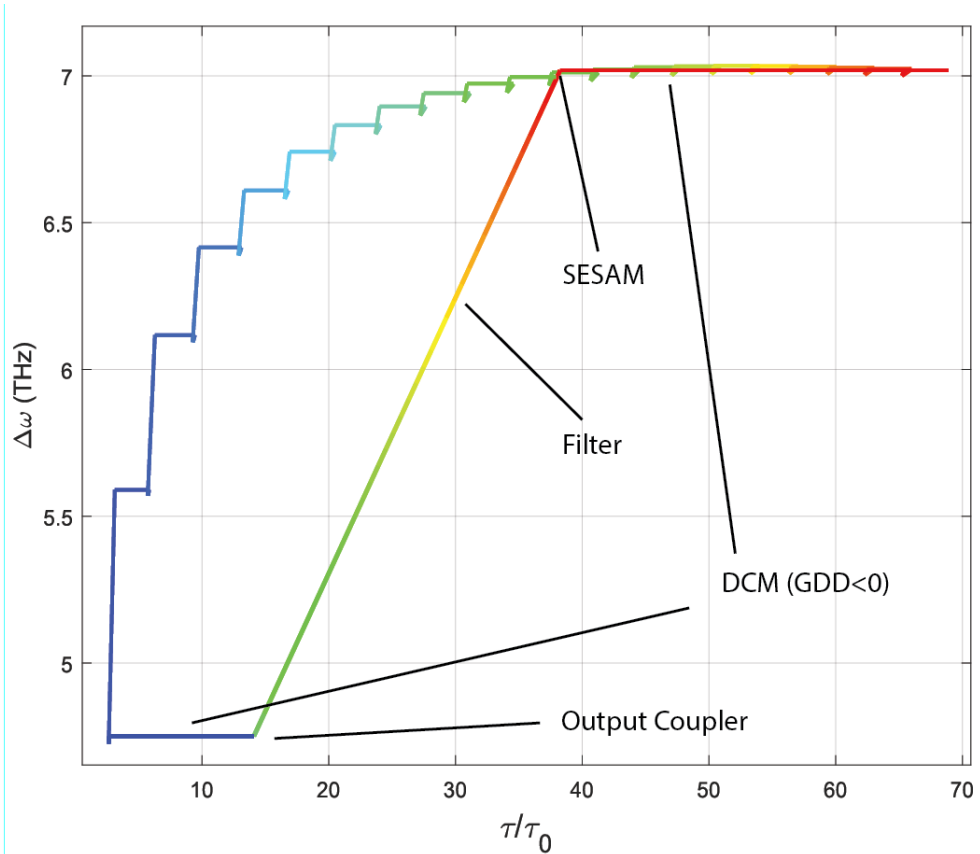


Figure 5.5: Phase space plot of discrete similariton after the pulse stabilizes.

Here, we present an algorithm for generating Fresnel holograms that can project high-quality back-to-back images in multiple planes [55]. The method utilizes adaptive-additive iterative Fourier transform algorithm (IFTA), Fresnel zone plates (FZPs), superposition and the kinoform principle, used to generate a phase-type Fresnel hologram that projects multi-plane images. We will show that the method uses the inherent connection between Fresnel and Fourier holograms. So the algorithm can benefit from the established Fourier CGH techniques for generating the final Fresnel CGH. We demonstrated the proposed hologram with up to 11 layers of images experimentally. Then we showed the bottleneck in the number of layers in terms of cross-talk is not inherent to the algorithm, but the resolution of SLM, which makes this method promising with the emerging technologies of imaging and display.

The algorithm is described in Figure 5.7. We start with the images we want to

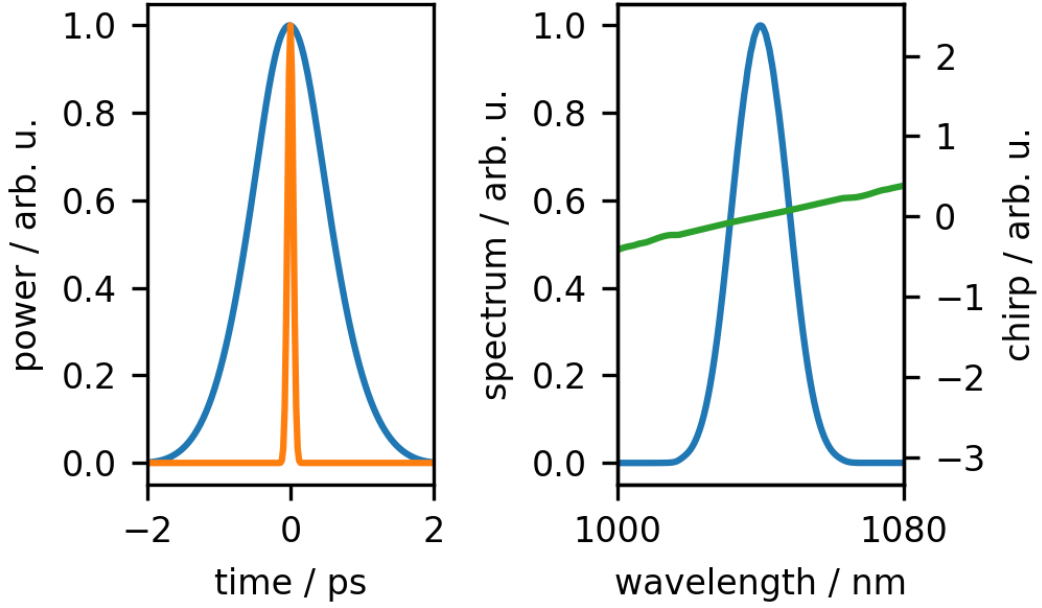


Figure 5.6: Similariton TDL: Temporal (left) and spectral (right) shape of pulses extracted after the spectrally shaped output coupler. The numerically dechirped and nearly transform-limited pulse is indicated in orange color. The chirp of the spectrum is indicated in green. Figure taken from [50]

project. First, a random phase is added to each image as preprocessing. Then, Fourier hologram of each image is generated with adaptive-additive IFTA. The phases of resulting holograms are superimposed with phases of FZPs to bring the images from infinity to any desired distance, converting them into Fresnel holograms. Finally, complex superimposing all calculated holograms with each other gives us a single complex hologram. We can extract the kinoform from the resulting complex hologram by extracting the phase of it.

The experimental setup consists of a laser source (1035nm, up to 300 mW), a spatial light modulator (SLM, Hamamatsu X10468-03, 800x600 resolution), screen, and digital camera (Canon, 60D): The hologram size is 512x512 pixels in all the experiments. We fixed the screen (Thorlabs VRC4) and the camera on a motorized stage to conserve the focus of the camera throughout the imaging. There are no lenses in the system except the telescope that is used to collimate

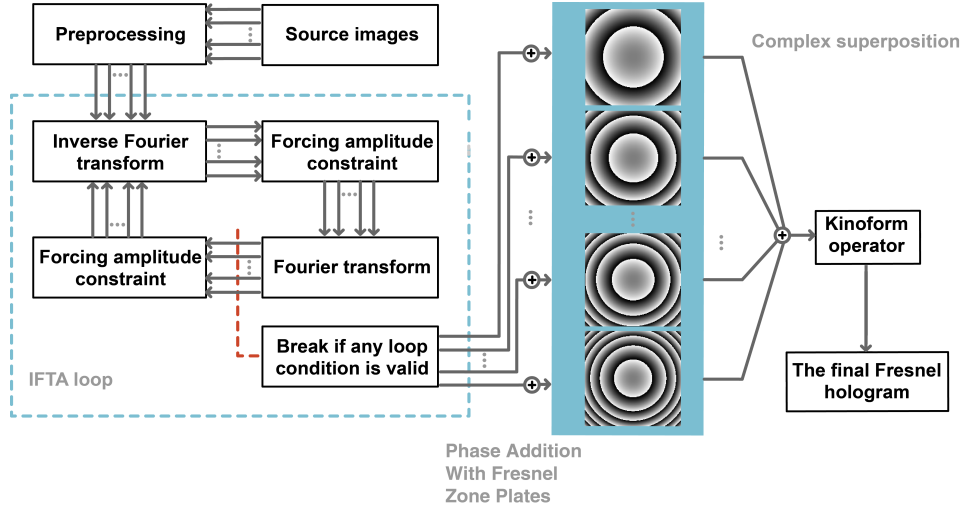


Figure 5.7: Flowchart of the proposed CGH algorithm. Fourier holograms of source images are calculated independently after preprocessing. Then, phases of each image are superimposed with phases of any desired FZPs. Finally, superimposing in complex form and taking the kinoform of the result gives us a single Fresnel hologram capable of projecting multiple planes.

the incoming beam. The optical reconstruction of “BILKENT UNIV” with back-to-back letters is shown in Figure 5.8. All images are constructed from 18 cm to 170 cm from SLM. Each image is well separated from each other to reduce the crosstalk between images, as it decreases the contrast of each image.

The main bottleneck for the maximum number of layers is resolution SLM. We can either decrease the complexity of images (number of active pixels in each source image), or as a better alternative, increase the resolution SLM. In Figure 5.9, we simulated a 3D model of a space ship. We sampled 100 slices from the space ship which are fed to the algorithm assuming 4000x4000 SLM. Resulting hologram is simulated at focal distances of each layer. Then the results of the simulations are combined together on the computer as a reconstruction of the 3D model.

Each image is calculated independently so the process can be parallelized. This reduces the calculation time roughly the same as calculation time for a single Fresnel hologram which takes most of the computation time. Since IFTA depends on Fourier transforms, carrying the computation of IFTA to GPU further

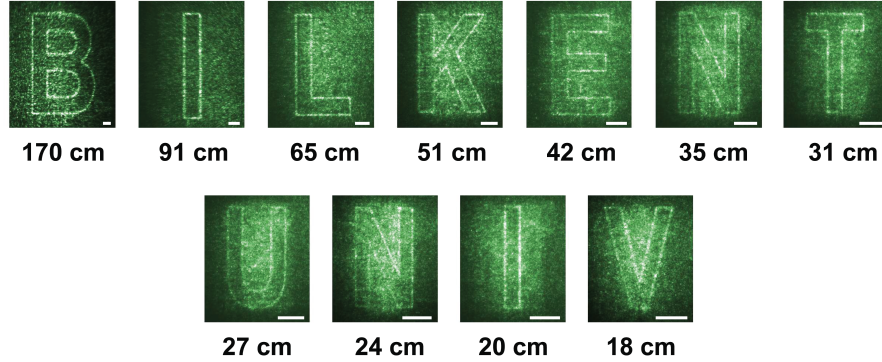


Figure 5.8: Optical Reconstruction of “BILKENT UNIV” with SLM. Letters are ordered from last to first with respect to SLM. The scale at the corner of each image is 5 mm distances from SLM can be seen below each image.

decreases the calculation times. We used a computer with Intel i5-7600 CPU and Nvidia GTX 1070 GPU to calculate 11 letters which were completed in 0.17 seconds.

The proposed method allows us to generate many layers of images with high flexibility over depth control with a single CGH. Further, the proposed method relies on already established and optimized IFTA which allows us to generate holograms in real time. We showed 11 back-to-back letters, each at controllable depths. In addition to that, we simulated 100 layers of a 3D model of a space ship rendered with 4K SLM. The proposed method can be used in many applications ranging from 3D microscopy to display technologies.

One such application can be in 3D printing, where projected 3D hologram can excite the medium, like photoresist. We speculate, with the help of the properties of ablation cooled regime shown here, 3D holograms can be used for fast and efficient 3D printing. Nonetheless, the interaction of pulses with each other should be studied further to confirm similar advantages translates to mechanics other than reduction of ablation threshold via heat profile engineering.

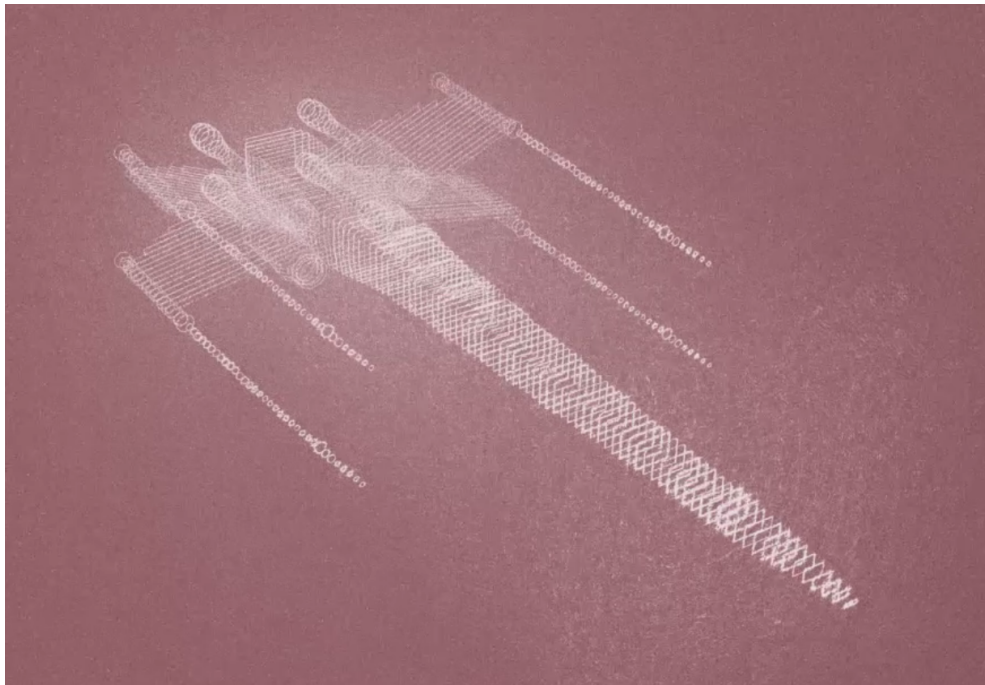


Figure 5.9: Computational reconstruction of 100 layers of a space ship by simulating a 4K SLM. Each layer is simulated at their focal point and then combined in 3D computationally.

Chapter 6

Conclusion

This thesis extended the work first introduced in [17] in terms of the limits and viability of the method. Scaling property of ablation cooled material removal is explored.

TTM simulations suggested there is ideal pulse energy for each repetition rate for every material. Further, it can be calculated using only the ablation threshold for a single pulse. Simulations also showed that scaling of ablation could be indefinite as the number of pulses each burst is increased. This result may not translate to reality exactly due to approximations made in our model. When one of the single burst simulations is visualized, the temperature profile of the material after ablation starts appears to reach a steady state where we can predict the depth of the ablation for next pulse from reduced ablation threshold. So, by engineering this profile, it should be possible to increase the ablation depth while keeping the residual heat minimal.

The simulation results were confirmed with experiments done on two different materials using three laser systems. First set of experiments done with 1.6 GHz pulse repetition rate confirmed the outcomes of the simulations. Then, 1.46 GHz system is used to test how different beam and pulse parameters behaved while keeping a comparable pulse repetition rate. As expected, the ablation threshold

is decreased when the beam is focused more which in turn reduced heating. The first ablation on dentin without any carbonization was achieved using this system. The limits of ablation cooling were pushed using 13 GHz system. Some ablation occurred at 5 nJ while consistent ablation is accomplished using 15 nJ pulses compared to 80 nJ in 1.6 GHz system even though both lasers have the same pulse duration and spot size. As pulse energy increases, both ablated depth and area of melting increased.

One possible improvement to all experiments in shaping the beam to decrease melting is using beam shaping. A straight forward shape is a top hat though not the best necessarily. Additionally, the ablation efficiency and reduction of heat can be improved by engineering the pulse energies inside a burst individually. The ideal temperature gradient would be a step function dropping around penetration depth of laser to the material. This way, each pulse would ablate some while keeping the temperature gradient the same after ablation. Another improvement can be made by increasing the pulse energies of the first few pulses that fail to ablate. So a better portion of the burst can contribute to the ablation which in turn would increase the efficiency of bursts.

Possibly, the temporal features of GHz repetition rates will be of use for imaging, detection and sensing techniques too. Shaping the envelope of bursts combined with nonlinear interaction between pulses is not yet explored in other fields. As a result, lasers can become even more critical with every aspect of science, industry, and medicine.

Finally, studies that possibly can be implemented in conjunction with this thesis are presented. They still can contribute to in tandem with the engineering temperature gradient. The discrete similariton and dissipative soliton for thin-disk lasers can potentially be used for ablation cooled material removal by themselves. So, the pulse energy produced by a thin disk oscillator at high repetition rates would render any amplification after that unnecessary. A material processing system with the only oscillator would decrease cost and complexity along with advantages of ablation cooled regime.

High-density 3D holograms can be accompanied by ablation cooling to ablate any complex volumetric pattern extremely fast. Alternatively, the same methods can be used for 3D printing without any ablation since many of them depend on nonlinear optical absorption too. It works by imprinting diffusion on each hologram layer. That increases the degree of freedom which in turn lowers the most challenging problem of multi-layer holograms, cross-talk. Additionally, the algorithm is based on IFTA which is already highly optimized. As a result, real-time generation of hundreds of layers is possible with current, consumer-grade hardware.

The implication of engineering temperature gradient with pulses around a few tens of nJ energy is to eliminate the need for chirped pulse amplification. The concerns over nonlinearity during and after amplification vanish when dealing with such low energies. Considering chirped pulse amplification is recently awarded with Nobel prize in physics, the implications of such progress become much more pronounced. Current femtosecond laser technology can change drastically towards higher repetition rates with reduced complexity instead of pushing for greater pulse energies. Even lasers without any amplification stages can emerge which tend to have cleaner pulse shapes after superficial compression. Other benefits such as reduced heating and increased processing speeds only add to the value of ablation cooled regime.

Bibliography

- [1] T. H. Maiman *et al.*, “Stimulated optical radiation in ruby,” 1960.
- [2] B. P. e. a. Abbott, “Gw170104: Observation of a 50-solar-mass binary black hole coalescence at redshift 0.2,” *Phys. Rev. Lett.*, vol. 118, p. 221101, Jun 2017.
- [3] C. Weitkamp, *Lidar: range-resolved optical remote sensing of the atmosphere*, vol. 102. Springer Science & Business, 2006.
- [4] A. Abramovici, W. E. Althouse, R. W. P. Drever, Y. Gürsel, S. Kawamura, F. J. Raab, D. Shoemaker, L. Sievers, R. E. Spero, K. S. Thorne, R. E. Vogt, R. Weiss, S. E. Whitcomb, and M. E. Zucker, “Ligo: The laser interferometer gravitational-wave observatory,” *Science*, vol. 256, no. 5055, pp. 325–333, 1992.
- [5] M. Deubel, G. Von Freymann, M. Wegener, S. Pereira, K. Busch, and C. M. Soukoulis, “Direct laser writing of three-dimensional photonic-crystal templates for telecommunications,” *Nature materials*, vol. 3, no. 7, p. 444, 2004.
- [6] P. J. Keller, A. D. Schmidt, J. Wittbrodt, and E. H. Stelzer, “Reconstruction of zebrafish early embryonic development by scanned light sheet microscopy,” *science*, vol. 322, no. 5904, pp. 1065–1069, 2008.
- [7] S. Mukamel, *Principles of nonlinear optical spectroscopy*, vol. 29. Oxford university press New York, 1995.

- [8] A. Ashkin, J. M. Dziedzic, J. Bjorkholm, and S. Chu, “Observation of a single-beam gradient force optical trap for dielectric particles,” *Optics letters*, vol. 11, no. 5, pp. 288–290, 1986.
- [9] J. Powell, *CO2 laser cutting*, vol. 214. Springer, 1993.
- [10] V. Coffey, “High-energy lasers: new advances in defense applications,” *Optics and Photonics News*, vol. 25, no. 10, pp. 28–35, 2014.
- [11] R. O’Rourke, “Navy shipboard lasers for surface, air, and missile defense: Background and issues for congress,” LIBRARY OF CONGRESS WASHINGTON DC CONGRESSIONAL RESEARCH SERVICE, 2013.
- [12] P. M. Livingston and A. D. Schnurr, “Laser anti-missile defense system,” Mar. 30 1993. US Patent 5,198,607.
- [13] K. D. Solomon, L. E. F. de Castro, H. P. Sandoval, J. M. Biber, B. Groat, K. D. Neff, M. S. Ying, J. W. French, E. D. Donnenfeld, R. L. Lindstrom, *et al.*, “Lasik world literature review: quality of life and patient satisfaction,” *Ophthalmology*, vol. 116, no. 4, pp. 691–701, 2009.
- [14] J. R. Lakowicz, *Principles of fluorescence spectroscopy*. Springer Science & Business Media, 2013.
- [15] M. W. Berns, J. Edwards, K. Strahs, J. Girton, P. McNeill, J. Rattner, M. Kitzes, M. Hammer-Wilson, L. Liaw, A. Siemens, *et al.*, “Laser microsurgery in cell and developmental biology,” *Science*, vol. 213, no. 4507, pp. 505–513, 1981.
- [16] R. Cubeddu, A. Pifferi, P. Taroni, A. Torricelli, and G. Valentini, “A solid tissue phantom for photon migration studies,” *Physics in Medicine and Biology*, vol. 42, no. 10, p. 1971, 1997.
- [17] C. Kerse, H. Kalaycıoğlu, P. Elahi, B. Çetin, D. K. Kesim, Ö. Akçaalan, S. Yavaş, M. D. Aşık, B. Öktem, H. Hoogland, R. Holzwarth, and F. Ö. Ilday, “Ablation-cooled material removal with ultrafast bursts of pulses,” *Nature*, vol. 537, pp. 84 – 88, jul 2016.

- [18] D. Sands, “Pulsed Laser Heating and Melting,” *Heat Transfer - Engineering Applications*, p. 25, 2011.
- [19] W. M. Rohsenow, J. P. Hartnett, Y. I. Cho, *et al.*, *Handbook of heat transfer*, vol. 3. McGraw-Hill New York, 1998.
- [20] M. Knowles, G. Rutterford, D. Karnakis, and A. Ferguson, “Micro-machining of metals, ceramics and polymers using nanosecond lasers,” *The International Journal of Advanced Manufacturing Technology*, vol. 33, no. 1-2, pp. 95–102, 2007.
- [21] M. Perry, B. Stuart, P. Banks, M. Feit, V. Yanovsky, and A. Rubenchik, “Ultrashort-pulse laser machining of dielectric materials,” *Journal of applied physics*, vol. 85, no. 9, pp. 6803–6810, 1999.
- [22] D. F. Swinehart, “The Beer-Lambert Law,” *Journal of Chemical Education*, vol. 39, p. 333, 2009.
- [23] B. Stuart, M. Feit, S. Herman, A. Rubenchik, B. Shore, and M. Perry, “Nanosecond-to-femtosecond laser-induced breakdown in dielectrics,” *Physical Review B*, vol. 53, no. 4, p. 1749, 1996.
- [24] D. Strickland and M. Gerard, “Compression of amplified chirped optical pulses,” *Optics Communications*, vol. 56, no. 3, pp. 219–221, 1985.
- [25] E. Treacy, “Optical pulse compression with diffraction gratings,” *IEEE Journal of Quantum Electronics*, vol. QE-5, no. 9, pp. 454–458, 1969.
- [26] M. H. Niemz, *Laser-tissue interactions: fundamentals and applications*. Springer Science & Business Media, 2013.
- [27] S. Nikumb, Q. Chen, C. Li, H. Reshef, H. Zheng, H. Qiu, and D. Low, “Precision glass machining, drilling and profile cutting by short pulse lasers,” *Thin Solid Films*, vol. 477, no. 1-2, pp. 216–221, 2005.
- [28] R. R. Gattass and E. Mazur, “Femtosecond laser micromachining in transparent materials,” *Nature Photonics*, vol. 2, no. 4, pp. 219–225, 2008.

- [29] H. Lubatschowski, R. R. Krueger, and D. Smadja, *Textbook of Refractive Laser Assisted Cataract Surgery (ReLACS)*. Springer New York, 2013.
- [30] A. Ancona, F. Röser, K. Rademaker, J. Limpert, S. Nolte, and A. Tünnermann, “High speed laser drilling of metals using a high repetition rate, high average power ultrafast fiber cpa system,” *Optics Express*, vol. 16, no. 12, pp. 8958–8968, 2008.
- [31] W. Hu, Y. C. Shin, and G. King, “Modeling of multi-burst mode picosecond laser ablation for improved material removal rate,” *Applied Physics A*, vol. 98, no. 2, pp. 407–415, 2010.
- [32] J. M. Vadillo, J. M. Fernández Romero, C. Rodríguez, and J. J. Laserna, “Effect of plasma shielding on laser ablation rate of pure metals at reduced pressure,” *Surface and Interface Analysis*, vol. 27, pp. 1009–1015, 1999.
- [33] C. Kerse, *Ablation Cooled Material Removal With Bursts of Ultrafast Pulses*. PhD thesis, Bilkent University, 2016.
- [34] D. K. Kesim, *Application of ablation cooling technique to cataract surgery using all-fibre burst-mode laser*. PhD thesis, Bilkent University, 2016.
- [35] R. S. Marjoribanks, C. Dille, J. E. Schoenly, L. Mckinney, P. Kaifosh, P. Forrester, and Z. Qian, “Ablation and thermal effects in treatment of hard and soft materials and biotissues using ultrafast-laser pulse-train bursts,” *Photonics and Lasers in Medicine*, vol. 1, no. 3, pp. 155–169, 2012.
- [36] M. Lapczynna, K. Chen, P. Herman, H. Tan, and R. Marjoribanks, “Ultra high repetition rate (133mhz) laser ablation of aluminum with 1.2-ps pulses,” *Applied Physics A*, vol. 69, p. S883, 1999.
- [37] T. Qiu and C. Tien, “Heat transfer mechanisms during short-pulse laser heating of metals,” *Journal of Heat Transfer*, vol. 115, no. 4, pp. 835–841, 1993.
- [38] F. Vidal, T. Johnston, S. Laville, O. Barthélemy, M. Chaker, B. Le Drogoff, J. Margot, and M. Sabsabi, “Critical-point phase separation in laser ablation of conductors,” *Physical review letters*, vol. 86, no. 12, p. 2573, 2001.

- [39] I. Okuda and M. Shaw, “Gain depletion due to amplified spontaneous emission in multi-pass laser amplifiers,” *Applied Physics B*, vol. 54, no. 6, pp. 506–512, 1992.
- [40] J. Petelin, B. Podobnik, *et al.*, “Burst shaping in a fiber-amplifier chain seeded by a gain-switched laser diode,” *Applied optics*, vol. 54, no. 15, pp. 4629–4634, 2015.
- [41] C. J. Saraceno, F. Emaury, C. Schriber, A. Diebold, M. Hoffmann, M. Golling, T. Südmeyer, and U. Keller, “Toward millijoule-level high-power ultrafast thin-disk oscillators,” *IEEE Journal of Selected Topics in Quantum Electronics*, vol. 21, no. 1, pp. 106–123, 2015.
- [42] F. Kärtner and U. Keller, “Stabilization of solitonlike pulses with a slow saturable absorber,” *Optics letters*, vol. 20, no. 1, pp. 16–18, 1995.
- [43] D. E. Spence, P. N. Kean, and W. Sibbett, “60-fsec pulse generation from a self-mode-locked ti: sapphire laser,” *Optics letters*, vol. 16, no. 1, pp. 42–44, 1991.
- [44] F. Ö. Ilday and F. W. Wise, “Nonlinearity management: a route to high-energy soliton fiber lasers,” *JOSA B*, vol. 19, no. 3, pp. 470–476, 2002.
- [45] G. Palmer, M. Schultze, M. Siegel, M. Emons, U. Bünting, and U. Morgner, “Passively mode-locked yb: Klu (wo 4) 2 thin-disk oscillator operated in the positive and negative dispersion regime,” *Optics letters*, vol. 33, no. 14, pp. 1608–1610, 2008.
- [46] C. J. Saraceno, F. Emaury, C. Schriber, M. Hoffmann, M. Golling, T. Südmeyer, and U. Keller, “Ultrafast thin-disk laser with 80 μ j pulse energy and 242 w of average power,” *Optics letters*, vol. 39, no. 1, pp. 9–12, 2014.
- [47] J. Zhang, J. Brons, N. Lilienfein, E. Fedulova, V. Pervak, D. Bauer, D. Sutter, Z. Wei, A. Apolonski, O. Pronin, *et al.*, “260-megahertz, megawatt-level thin-disk oscillator,” *Optics letters*, vol. 40, no. 8, pp. 1627–1630, 2015.

- [48] W. Renninger, A. Chong, and F. Wise, “Dissipative solitons in normal-dispersion fiber lasers,” *Physical Review A*, vol. 77, no. 2, p. 023814, 2008.
- [49] F. Ilday, J. Buckley, W. Clark, and F. Wise, “Self-similar evolution of parabolic pulses in a laser,” *Physical review letters*, vol. 92, no. 21, p. 213902, 2004.
- [50] F. . Ilday, D. K. Kesim, M. Hoffmann, and C. J. Saraceno, “Discrete similariton and dissipative soliton modelocking for energy scaling ultrafast thin-disk laser oscillators,” *IEEE Journal of Selected Topics in Quantum Electronics*, vol. 24, pp. 1–12, Sep. 2018.
- [51] L. L. Yuan and P. R. Herman, “Laser scanning holographic lithography for flexible 3d fabrication of multi-scale integrated nano-structures and optical biosensors,” *Scientific reports*, vol. 6, p. 22294, 2016.
- [52] O. Tokel, A. Turnalı, G. Makey, P. Elahi, T. Çolakoglu, E. Ergeçen, Ö. Yavuz, R. Hübner, M. Z. Borra, I. Pavlov, *et al.*, “In-chip microstructures and photonic devices fabricated by nonlinear laser lithography deep inside silicon,” *Nature photonics*, vol. 11, no. 10, p. 639, 2017.
- [53] Z. Yang, Q. Fan, Y. Zhang, J. Liu, and J. Zhou, “A new method for producing computer generated holograms,” *Journal of Optics*, vol. 14, no. 9, p. 095702, 2012.
- [54] A. A. Gülses and B. K. Jenkins, “Cascaded diffractive optical elements for improved multiplane image reconstruction,” *Applied optics*, vol. 52, no. 15, pp. 3608–3616, 2013.
- [55] G. Makey, Ö. Yavuz, D. K. Kesim, A. Turnalı, P. Elahi, S. Ilday, O. Tokel, and F. Ö. Ilday, “Breaking crosstalk limits to dynamic holography using orthogonality of high-dimensional random vectors,” *Nature Photonics*, vol. 13, no. 4, pp. 251–256, 2019.
- [56] L. M. Frantz and J. S. Nodvik, “Theory of pulse propagation in a laser amplifier,” *Journal of Applied Physics*, vol. 34, no. 8, pp. 2346–2349, 1963.

Appendix A

Laser Systems

A.1 1.6 GHz Non-PM System

Amplifier stages are seeded with 100 MHz dispersion managed (DM) fiber oscillator A.1.

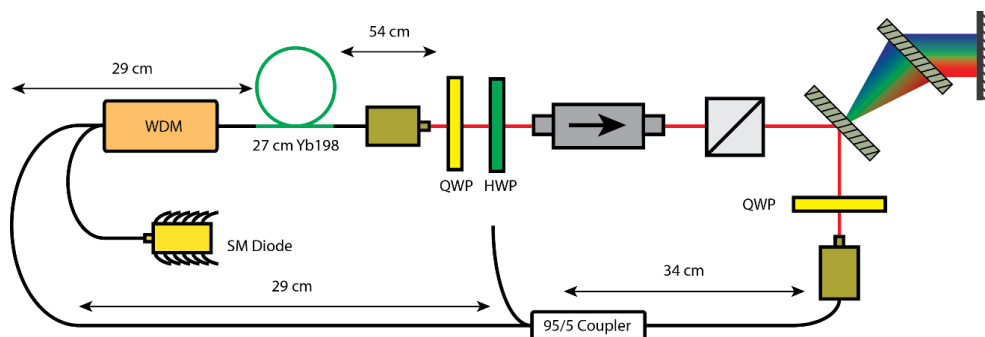


Figure A.1: Schematic of DM oscillator.

Output spectrum of the oscillator is taken from rejection port of PBS. Spectral width is 23 nm A.2 with 24 mW average power.

Output of oscillator is coupled in to the fiber via collimator. All the stages afterwards was built using non-PM fibers. After stretching pulses with 67 m stretch fiber, pulses are amplified with a single mode diode and Yb125 (4/125)

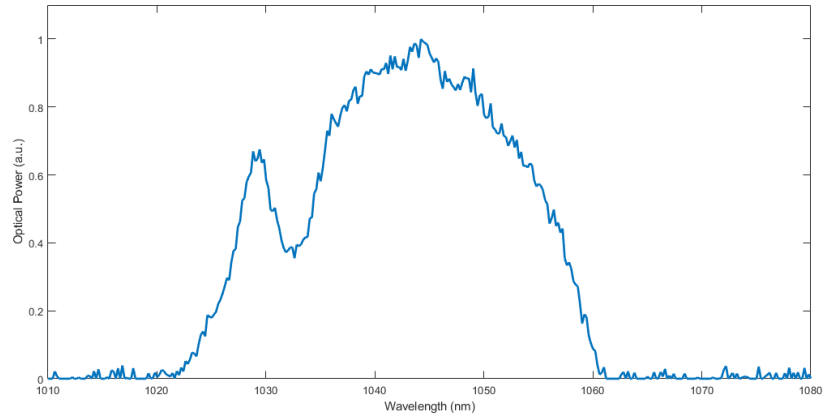


Figure A.2: Spectrum of the output of 100 MHz DM oscillator.

fiber. Then AOM picks the bursts via arbitrary waveform generator.

Two stages of single clad amplifiers compensate for the losses at AOM by increasing the average power to 500 mW. Then, a double clad power amplifier with wavelength stabilized multimode diode amplifies the power up to 4 W.

Finally, 5.8 m of Yb1200 25/250 DC fiber with two 55W diodes amplifies the pulses up to 120 nJ energy. Fiber is spliced to a 200 W isolator collimator. A 600 lines/mm grating pair compresses the pulses down to 350 fs FWHM. However, due to polarization and third order dispersion, effective width of the pulses are 1-2 ps. The corrected envelope for maximum number of pulses at highest energy is at Figure A.5.

Maximum power of the laser is 45 W. 50 % of the power is lost at grating compressor due to randomized polarization of the output. Then, another 5-7 % is lost after the galvo scanner. On sample, we can have 20 W average power to be used for processing. The scanning lens we used has 56 mm working distance where the beam can be focused down to 23 μm .

A.2 1.46 GHz PM System

Design of the cataract surgery system [34] is modified for higher repetition rates. A repetition rate multiplier is placed after AOM to achieve 1.46 GHz from 89 MHz oscillator. This allows for precise pulse picking through AOM while sacrificing pulse energy after it. Two stages of amplification compensates for that. After stretching, pulses are amplified since AOM will reject most of the pulses. Finally, two stages high power amplifiers are used in series to reach 15 W average power. Last stage of amplifier is pumped with a 976 nm and 915 nm pump diodes simultaneously to reduce gain depletion while achieving significant powers.

After compressing the pulses with 900 lines/mm grating compressor, we end up with 250-300 fs lorentzian pulses. The output is coupled to Thorlabs galvo scanner. Focusing lens is LSM02-BB which has 18 mm working distance and is able to focus beam down to 11 μm spot diameter. Diodes of the laser power amplifier can be modulated optionally to amplify any number of bursts selectively. The compressed pulse and output spectrum can be seen from Figure A.8a and A.8b respectively.

A.3 13 GHz Prechirped System

The third laser is constructed with prechirping instead of compressing after collimator which can be seen in Figure A.9. Even though this scheme can't compress pulses to femtosecond range, not losing any power at compressor is much more necessary for experiments.

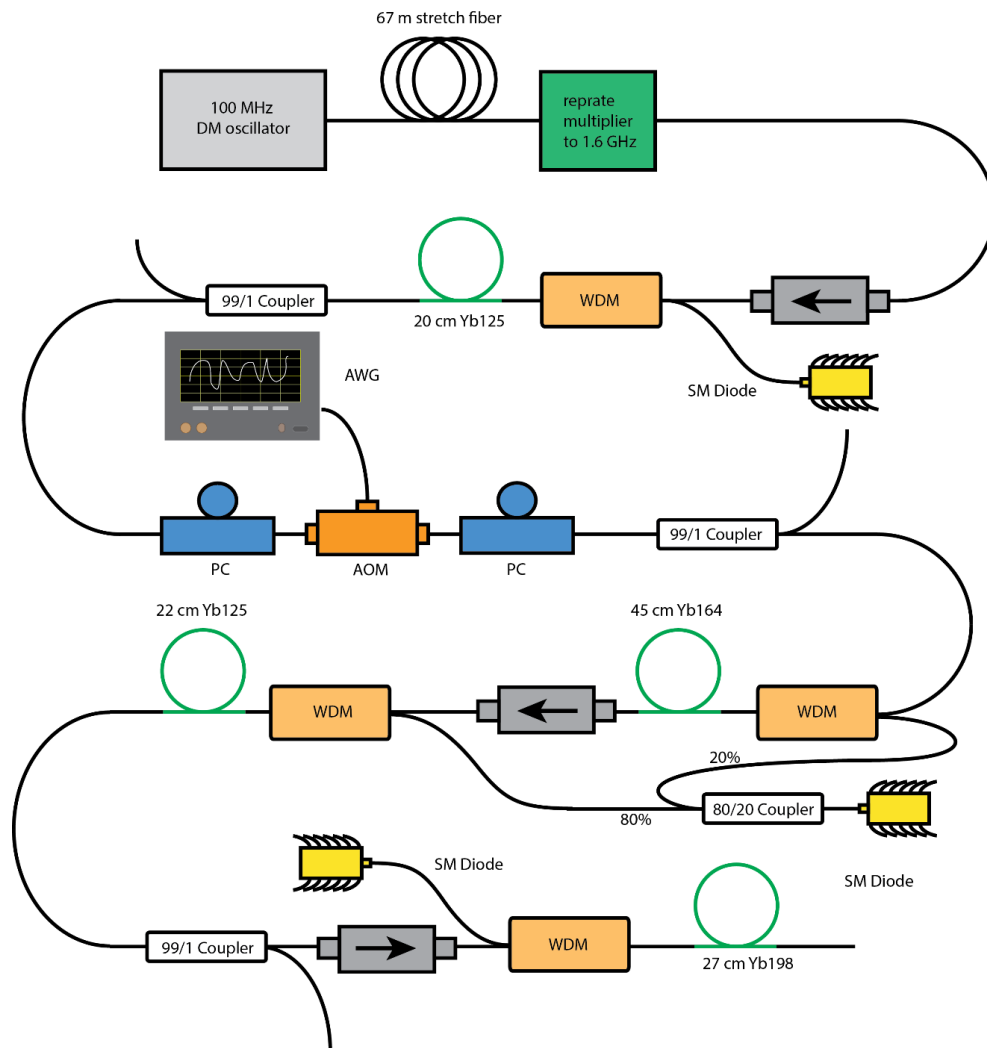


Figure A.3: The general schematic of the 1.6 GHz laser. Amplifiers are seeded by 100 MHz DM oscillator. After stretching the pulses, replate multiplier is used to increase the pulse repetition rate to 1.6 GHz. AOM is modulated with an arbitrary waveform generator to compensate for gain depletion.

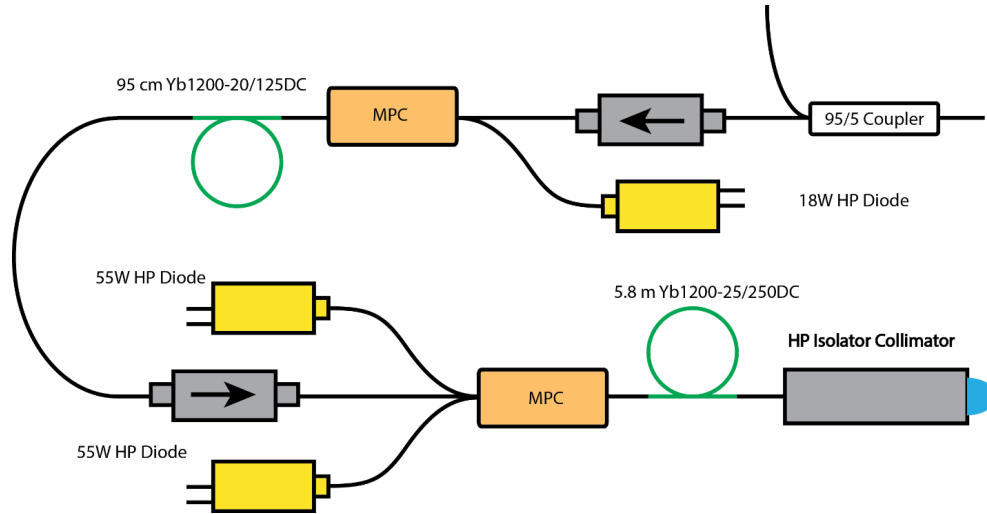


Figure A.4: In the final stage, two double clad amplifiers are cascaded. The first one amplifies up to 5 W average power with a wavelength stabilized 18 W diode. Second one is coupled with two 55 W 976 nm diodes to achieve 52 W average power.

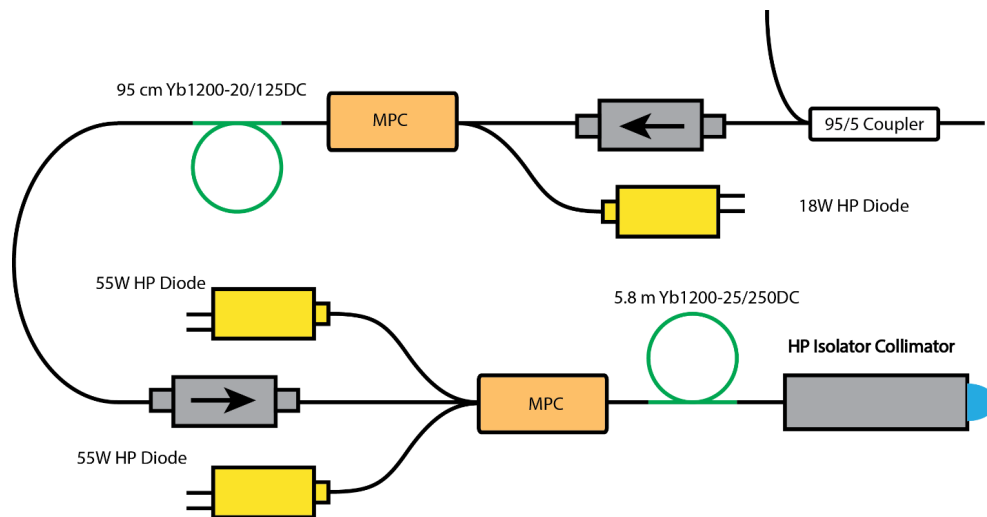
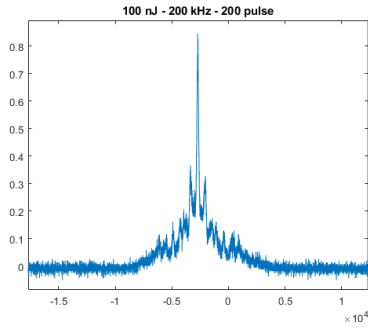
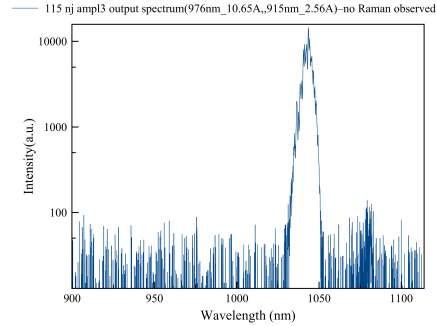


Figure A.5: The burst envelope for 1000 pulses per burst with 100 nJ pulses.



(a) Autocorrelation of 90 nJ pulses. Side peaks vanish when pulse energy drops below 50 nJ.



(b) Spectrum of the output of laser at 90 nJ. Raman amplification starts to become prominent if pulses are amplified further.

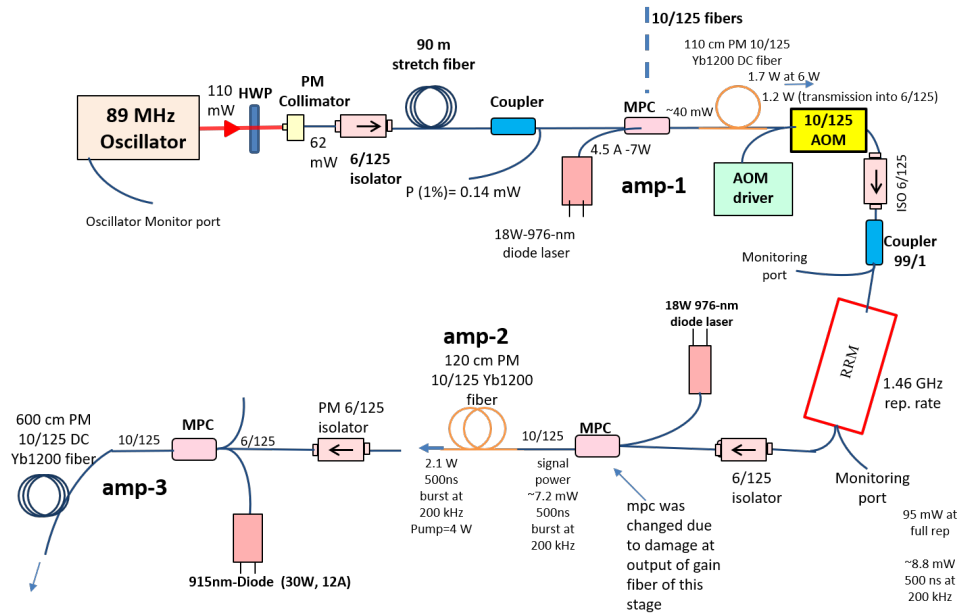
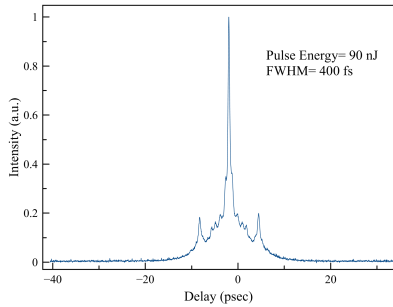
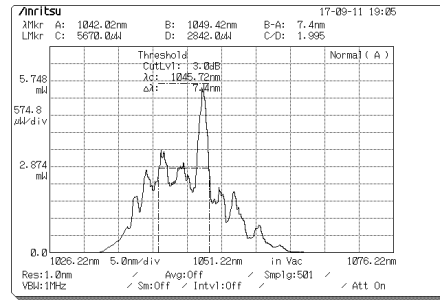


Figure A.7: 1.46 GHz laser schematic. Amplifier stages are seeded with 89 MHz ANDi oscillator. Power at each stage can be seen above.



(a) Autocorrelation of 100 nJ pulses.



(b) Spectrum of the output of laser at 100 nJ. Modulations are due to non-polarized beam, passing through grating.

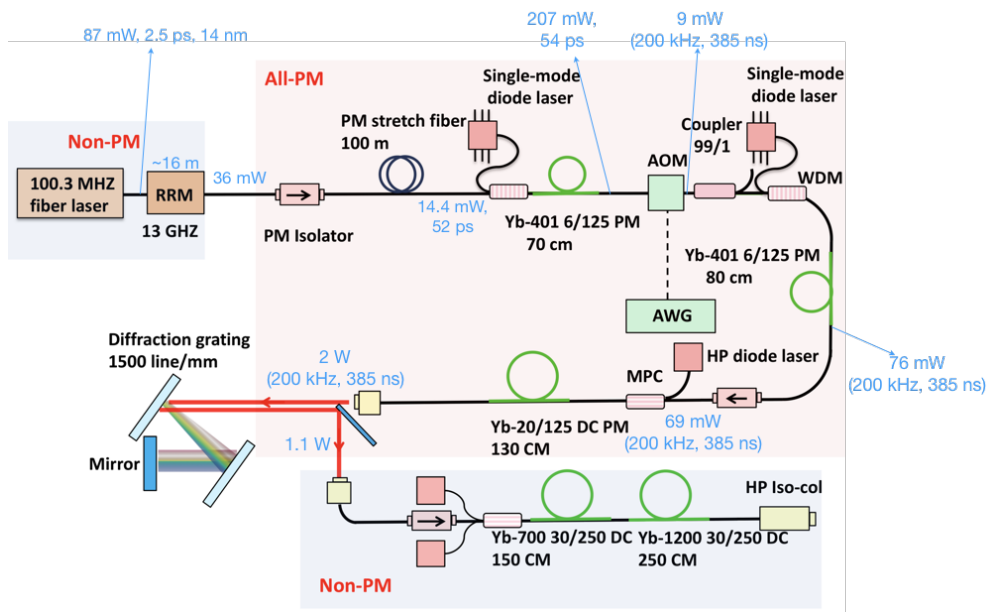


Figure A.9: 13 GHz laser schematic. Amplifier stages are seeded with 100 MHz ANDi oscillator. Power at each stage can be seen above.

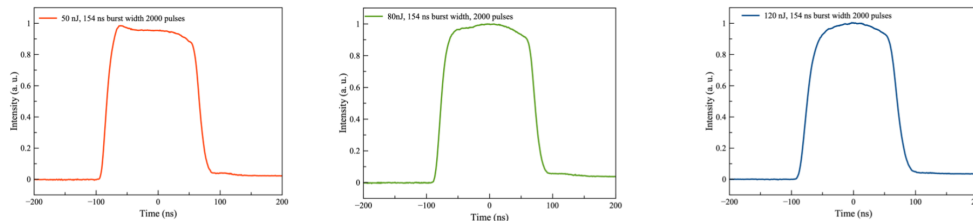


Figure A.10: The burst envelopes for 2000 pulses per burst for 50, 90 and 120 nJ pulse energies after modulating the AOM for modeled amplifier stages.

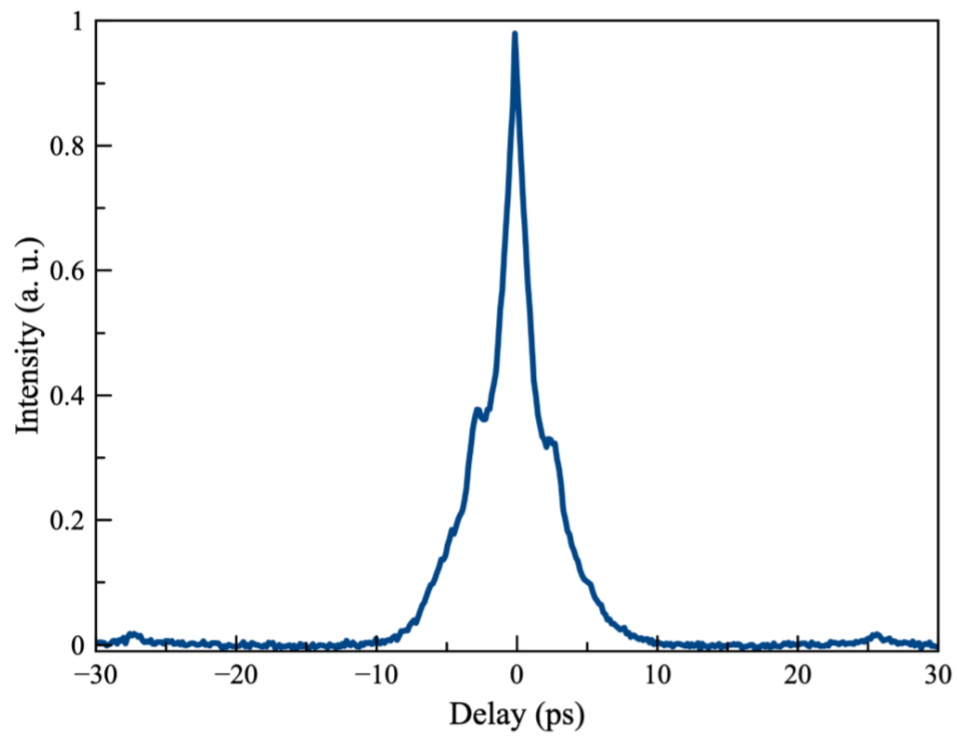


Figure A.11: Autocorrelation of the output pulses at 50 nJ.

Appendix B

Burst Envelope Shaping by Modelled Amplifiers

The relatively low repetition rate of bursts presents a well known issue called gain depletion where initial pulses of burst experience more gain compared to later ones due to the decrease in population inversion. This becomes especially prominent for applications presented in here since the burst durations are less than half period of burst repetition rate while extending to hundreds of nanoseconds.

The gain depletion accumulates with every stage of amplification. Since all systems used here consists of multiple amplifier stages, gain depletion becomes very disruptive. To fix those effects, the method presented in [40] is implemented.

Each stage of amplifier is modeled by Frantz-Nodvik pulse-amplification equations [56].

Since the pulse train before AOM does not matter, only amplifiers coming later are modeled. First, the input burst shape that will produce a flat burst for last amplifier stage is calculated. Then, the calculated shape is used to calculate the input at the previous stage of amplifier. By repeating this process until AOM is reached, the burst shape to be applied can be found.

The MATLAB implementation is given below. The response of AOM driver had to be adjusted manually in the form of offset.

B.1 MATLAB Implementation

```
1 clear;
2 close all;
3
4 %% constants
5
6 h = 6.626e-34; % Js Planck's constant
7 v = 2e8; % m/s speed of light inside fiber
8 n1 = 0.8; % coupling efficiency
9 n2 = 0.6;
10 nn = 0.7;
11 sigma = 0.65e-24; % m^2 stimulated emission cross section
12 lambda = 1.044e-6; %m central wavelength
13 tb = 500e-9; % s burst duration
14 t = 0:1e-9:tb; % s time
15
16 %% calculated constants
17
18 hbar = h/(2*pi);
19 omega = 2*pi*v;
20
21 %% Pulse Parameters
22
23 rebrate = 200e3; % Hz burst repetition rate
24 rebratep = 1600e6; % Hz pulse-to-pulse repetition rate
25 Ep = 200e-9; %J pulse energy
26
27 Np = tb*rebratep; % # of pulses
```

```

28 Eb = Np*Ep; % J burst energy
29 Pavg = Eb*reprate; % W average power
30
31 %% Amplifier Parameters
32
33 P1in = 18.8e-3; % W input of first amplifier
34 P2in = 155e-3; % W input of second amplifier
35 P3in = 4; % W input of third amplifier
36
37 Es1 = 3.68e-6;% 4e-6 % J
38 Es2 = 92e-6; %100e-6; % J
39 Esn = 144e-6; %156e-6; % J
40
41 gamman = Esn/(nn*Es2);
42 gamma2 = Es2/(n2*Es1);
43
44 %% 3rd stage
45
46 Einn = P3in/(reprate);
47
48 an = exp(Eb/Esn);
49 bn = 1;
50 f0 = exp(Eb*t/(Esn*tb));
51
52 Kn = (an-bn*exp(Einn/Esn))/(exp(Einn/Esn)-1);
53 gn = Kn+f0;
54
55 Pinn = Eb*f0./(tb*(f0+Kn));
56
57 plot(t,Pinn/max(Pinn))
58
59 %% 2nd stage
60

```

```

61 Ein2 = P2in/(reprate);
62
63 a2 = (Kn+an) ^ gamman;
64 b2 = (Kn+bn) ^ gamman;
65
66 K2 = (a2-b2*exp(Ein2/Es2))/(exp(Ein2/Es2)-1);
67 g2 = K2+(gn) . ^ gamman;
68 Pin2 = Pinn.*(1-K2./g2)/nn;
69
70 figure;
71 plot(t, Pin2/max(Pin2))
72
73 %% 1st stage
74
75 Ein1 = P1in/(reprate);
76
77 a1 = (K2+a2) ^ gamma2;
78 b1 = (K2+b2) ^ gamma2;
79
80 K1 = (a1-b1*exp(Ein1/Es1))/(exp(Ein1/Es1)-1);
81 g1 = K1+(g2) . ^ gamma2;
82 Pin1 = Pin2.*(1-K1./g1)/n2;
83 Pin1s = Pin1/max(Pin1);
84
85 %% Rescaling y between 0.3 and 1
86 yn = Pin1;
87 yn = yn/max(yn);
88 yn = yn - min(yn);
89 yn = yn/max(yn);
90 low_level = 0.462;
91 yn = yn + low_level/(1-low_level); % for shifting 0.45 (
    add 2/3 for 0.4) (add 1 for 0.5) (add 9/11 for 0.45)
92 yn = yn/max(yn);

```



```
93 Pin1s = yn;
94
95 %% Scale time between 0 and 1
96
97 t_scaled = t/tb;
98
99 %% plotting
100 figure;
101 plot(t,Pin1s)
102
103 %% Fitting
104 %f=fit(t',Pin1s','exp1')
105
106 hold on;
107 %p=plot(f,t,Pin1s);
108 hold off
```